CHAPTER 5

Results and Discussion

Analytical and Numerical models were used to validate and study flow field, electric field and particle trajectories inside equipments. The analytical model uses the mathematic equations as shown in Chapter 3, while the numerical model uses equations of COMSOL software. The domain size in COMSOL is important for correct simulation. Although high domain resolution shows correct calculation, but it is complex and takes long time. So, the first step in simulation was to find a minimum domain number. Then, the flow field, electric field and particle trajectory were simulated in the next step. In addition, the laboratory testing was used to validate the simulation results. Finally, the EPMM was used to measure PM in ambient air, and compared with the standard detectors, including the TEOM, the beta ray and the laser technique.

5.1 Characteristic of Air Conditioning Inlet Section

The sampling head shown in Figure 3.2 was calculated to have 6.78×10^{-4}, 9.07×10^{-4}, and 7.85×10^{-5} m^2 in cross section area from 3×10^{-3}, 1.75×10^{-2}, and 5×10^{-3} m in radius, respectively. So, the velocity were 0.369, 0.260 and 3.185 m/s at the inlet, inside, and outlet of the sampling head, respectively. While, the diffusion dryer in Figure 3.4 were calculated to have 7.85×10^{-5} and 8.04×10^{-4} m^2 in cross section area of the inlet/outlet and the inside radius (5×10^{-3} and 1.6×10^{-2} m), respectively. The velocity were 3.185 and 0.311 m/s at the inlet/outlet and inside, respectively. Mesh convergence was used to validate a domains number for selected a minimum domains. Figures 5.1 and 5.2 show mesh convergence method to find a minimun domain for this numerical study. Axial cut line in part (a) of Figures 5.1 and 5.2 are an assumed line. The average velocity can be found from the values in this cut line. The average velocity of the cutting line in Figure 5.1 (b) shows that the smaller mesh was unstable and it was stable at about 300,000 domains. But the average velocity of the diffusion dryer in Figure 5.2 (b) increased steadily and stable at about 200,000 domains. Mesh parameters that gave stable result of

this device were set in domain of geometric entity level, fluid dynamic condition and triangular type which have 3.01×10^5 and 1.98×10^5 domain elements for the sampling head and the diffusion dryer, respectively, shown in Figure 5.3.

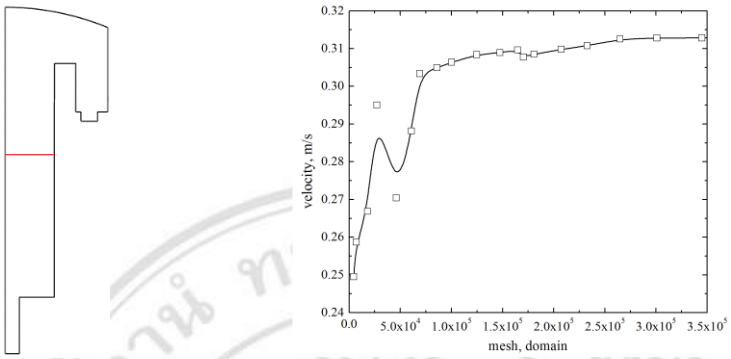

(a) Axial cut line for validation. (b) Velocity field average.

Figure 5.1 Mesh convergence curve of the sampling head model.

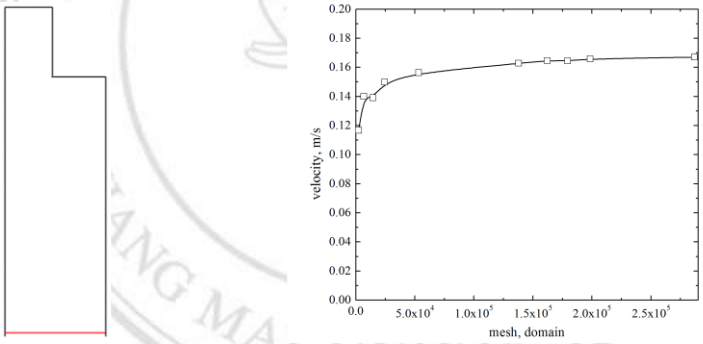

(a) Axial cut line for validation. (b) Velocity field average.

Figure 5.2 Mesh convergence curve of the diffusion dryer model.

(a) Feature of mesh domains in the sampling head.

(b) Feature of mesh domains in the diffusion dryer.

Figure 5.3 Mesh domains of the air inlet.

Figure 5.4 shows the velocity field inside the sampling head that has 0.76 s for aerosol residence time (calculated from 1.9×10^{-4} m^3 volume and 2.5×10^{-4} m^3/s or 15 L/min of aerosol flow rate). The sampling air is flowing inside and moving curve to the air exit. Most areas were laminar and the air exit area that has about 5.443 m/s in maximum velocity at the outlet, while the cross section axial of central cylindrical showed a low flow at the inner cylindrical surface and the center axis. When PM was put into the sampling head, it was found that all particle sizes showed similar movement, as shown in Figure 5.5. This simulation velocity showed a good laminar flow, low particle loss and suitable for prototype.

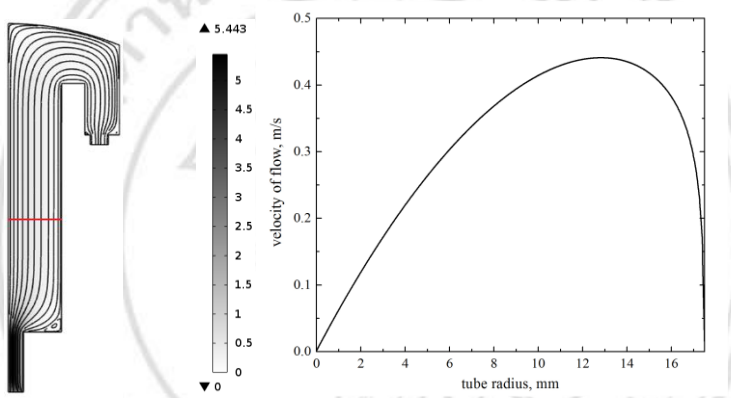

Figure 5.4 Velocity field inside the sampling head.

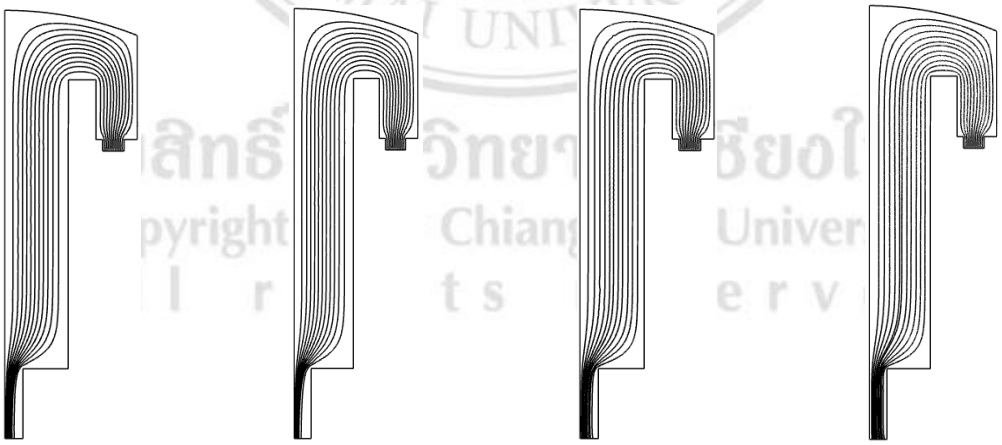

(a) PM100 (b) PM10 (c) PM2.5 (d) PM1.0

Figure 5.5 Particle Trajectories of PM100, PM10, PM2.5, and PM1.0.

The velocity field in the diffusion dryer is shown in Figure 5.6. It was found that the inside flow was laminar and regular at all areas. This flow can continuously absorb the RH from the aerosol sample with 3.2 s in residence time (calculated from 8×10^{-4} m^3

and 2.5×10^{-4} m^3/s or 15 L/min), while the cross section axial of central cylindrical showed a low flow at the inner cylindrical surface, and higher at the center axis. The flows from the inlet to the outlet were laminar, especially at inlet and outlet area which had low effect for pressure drop in the vacuum system.

The RH absorption efficiency was validated by the ambient air. The diffusion dryer measured the RH at the inlet/outlet and indoor/outdoor (Laboratory) from the ambient air for 5 and 15 L/min in flow rate, as shown in Figure 5.7. The RH of both flow rates were about 80 %RH and 64 %RH for outdoor and indoor ambient, respectively. The RH of the outdoor ambient air at the outlet or after pass the diffusion dryer was decreased to about 45 %RH for outdoor for 5 and 15 L/min, while, RH at the outlet from the indoor ambient air at 5 and 15 L/min was about 35 %RH. These results showed that this diffusion dryer was appropriate to use for removal of the RH in the air. In addition, the diffusion dryer was tested with the water spray, which can generate high RH about 98 %RH. The results shown in Figure 5.8 indicated that this diffusion dryer can reduce the RH down to about 50%RH at both flow rates of 5 and 15 L/min. The diffusion dryer can continuously reduce the RH. It was calculated to have about 45 % in absorbing efficiency, similar to the automatic diffusion dryer of Tuch *et al.* (2009). Although this efficiency was less than the DD250 diffusion dryer in Table 3.2, but it can be used at high flow rate and reduce the RH down to under 60 %RH. Figure 5.9 shows long time test for four days during 20 to 23 May 2016. It was found that the RH from the air ambient was reduced from about 60 %RH to about 35 %RH, shown in Figure 5.10. When the temperature effect was validate from the air ambient during 20 to 23 May 2016, it was found that the temperature difference was less than 1ºC (date 23 has rain) as shown in Figure 5.11. While, Figure 5.12 shows particle loss in the diffusion dryer when the NaCl aerosol was used. This test used 1.5 L/min aerosol flow rate and it was found that the NaCl of less than 100 nm in diameter showed high diffusion loss (about 16.67% loss at about 50 nm).

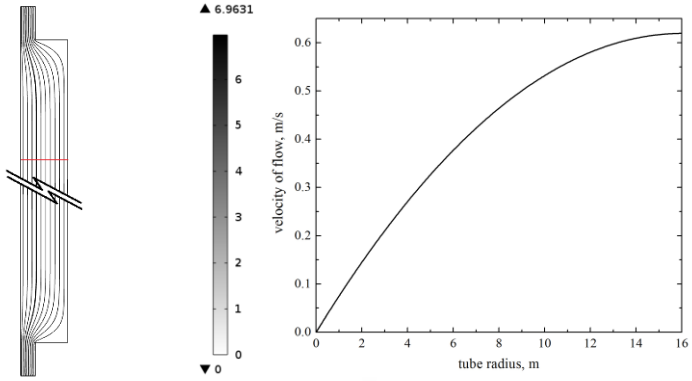

Figure 5.6 Flow field inside of the diffusion dryer.

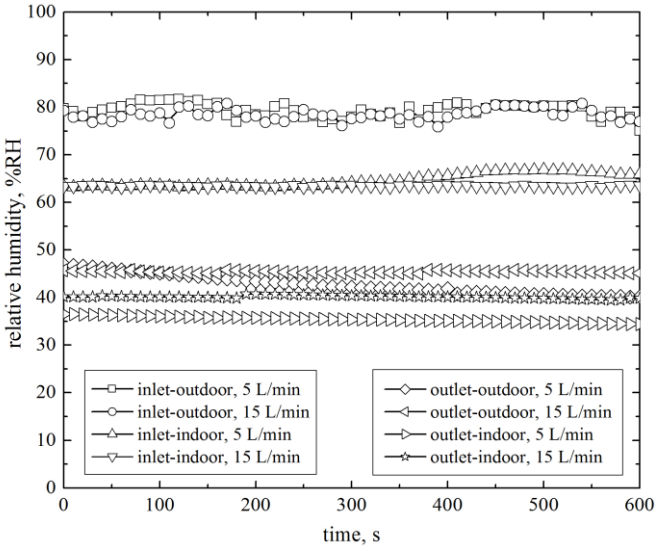

Figure 5.7 The RH from the air ambient.

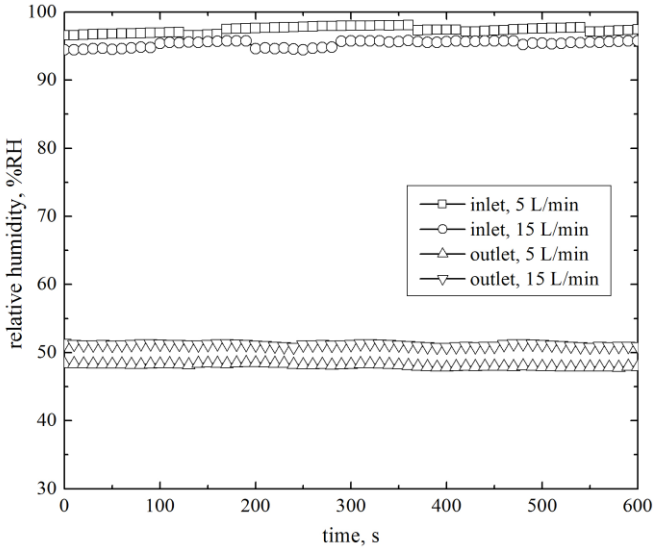

Figure 5.8 The RH from the water aerosol.

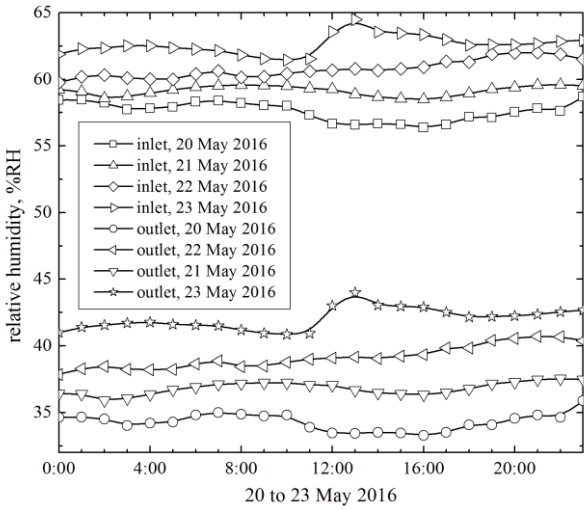

Figure 5.9 The RH of the ambient air.

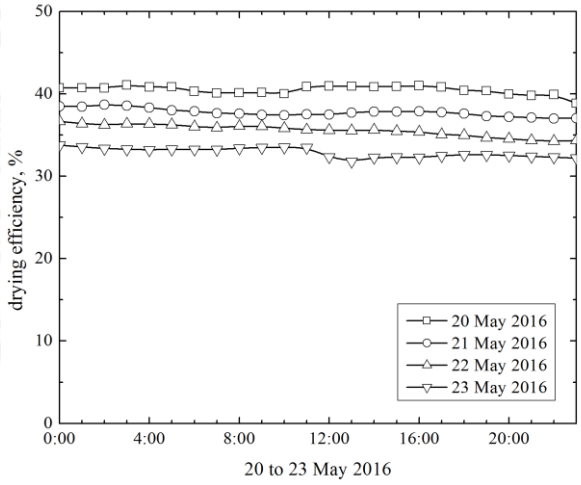

Figure 5.10 Drying efficiency of the diffusion dryer.

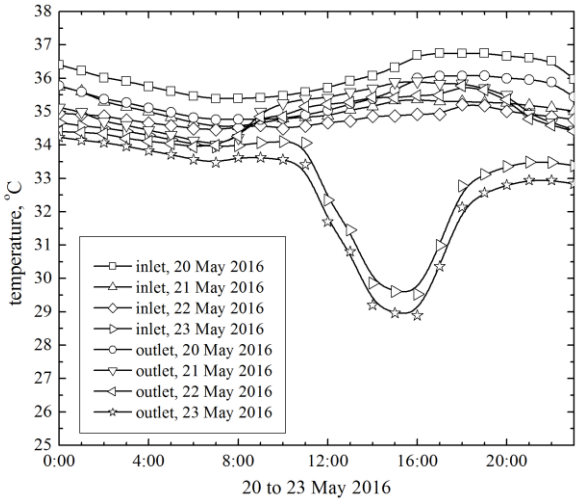

Figure 5.11 Temperature from the outdoor ambient air.

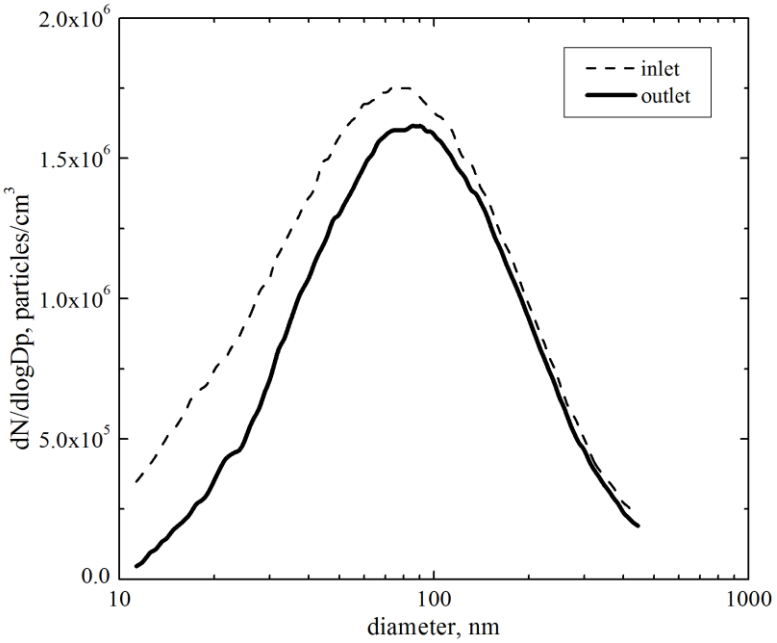

Figure 5.12 The NaCl particle loss between inlet and outlet of the diffusion dryer.

5.2 Characteristic of Particle Charging Section

Figure 5.13 (a) shows an axial cut line to find the average velocity in each of mesh domains. COMSOL was simulated in Figure 5.13 (b). It was found that the average velocity was increased and stable at about 80,000 mesh domains. So for simulation in this device, mesh parameter was set in geometric entity level, fluid dynamic condition and triangular type which have 1.05×10^5 domain elements, as shown in Figure 5.14. Electric field inside the particle charger showed difference in the ion trap voltage, shown in Figure 5.15 (a) and (b). At 0 V, the ion trap voltage had long electric field from the needle electrode to ion trap electrode. But at 300 V ion trap, the electric field was just short about the middle tube between the needle and ion trap electrode corresponding with experiment in an ion eletrostatic collector (Intra *et al.* 2014). Figures 5.16 and 5.17, it was found that the electric potential had diffusion at 300 V of the ion trap. Corresponding with electric field in Figure 5.18, electric field strength showed a maximum at the needle tip about 48,355 kV/m and decreased with distance. When the corona voltage was adjusted between 2.0 to 3.0 kV, it was found that the electric field strength was increased, shown in Figure 5.19. In case of the flow field, the velocity field in Figure 5.20 (a) shows laminar

flow, which is a good feature. The velocity field in Figure 5.20 (b) was high, in connecting tube area between the needle to the ion trap electrode.

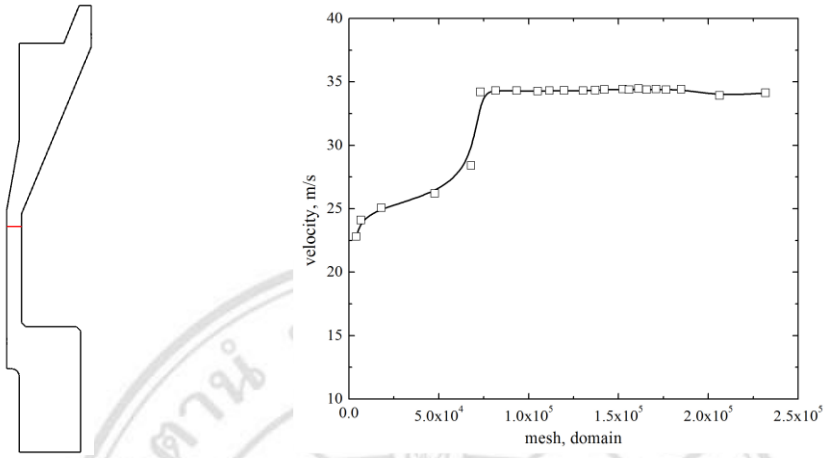

(a) Axial cut line for validation. (b) Velocity field average.

Figure 5.13 Mesh convergence curve of the particle charger model.

Figure 5.14 Feature of mesh domains in the particle charger.

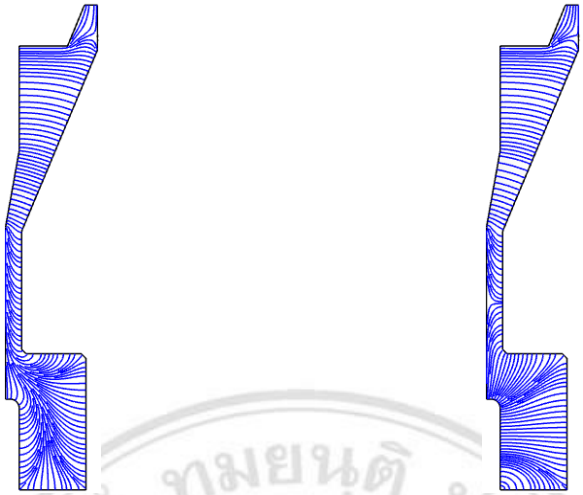

(a) Ion trap voltage = 0V (b) Ion trap voltage = 300V

Figure 5.15 Electric field inside the particle charger at 3 kV corona voltage.

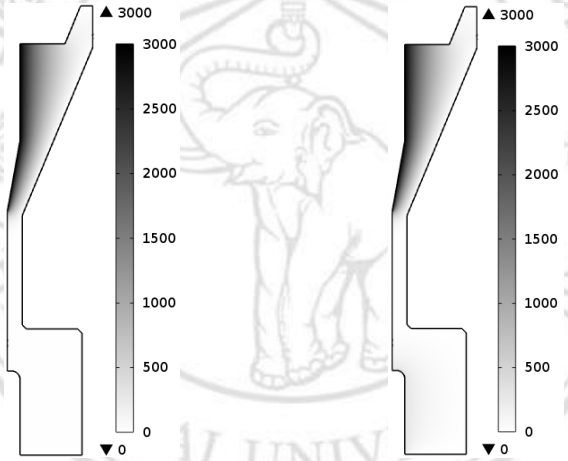

(a) Ion trap voltage = 0 V (b) Ion trap voltage = 300 V

Figure 5.16 Surface of electric potential inside the particle charger.

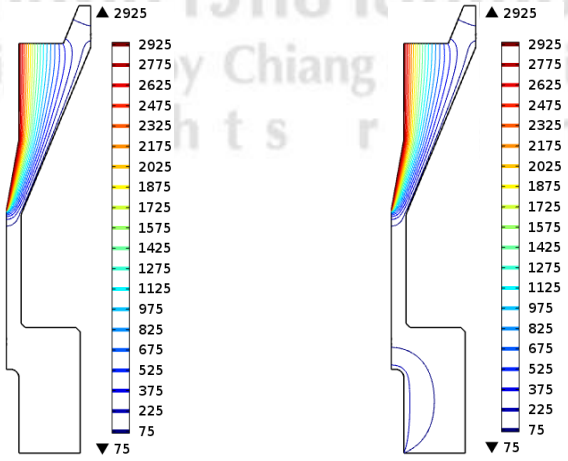

(a) Ion trap voltage = 0 V (b) Ion trap voltage = 300 V

Figure 5.17 Contour of electric potential inside the particle charger.

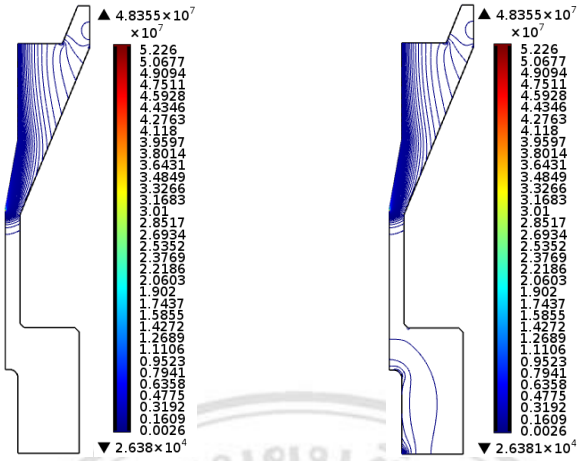

(a) Ion trap voltage = 0 V (b) Ion trap voltage = 300 V

Figure 5.18 Contour of electric field inside the charger.

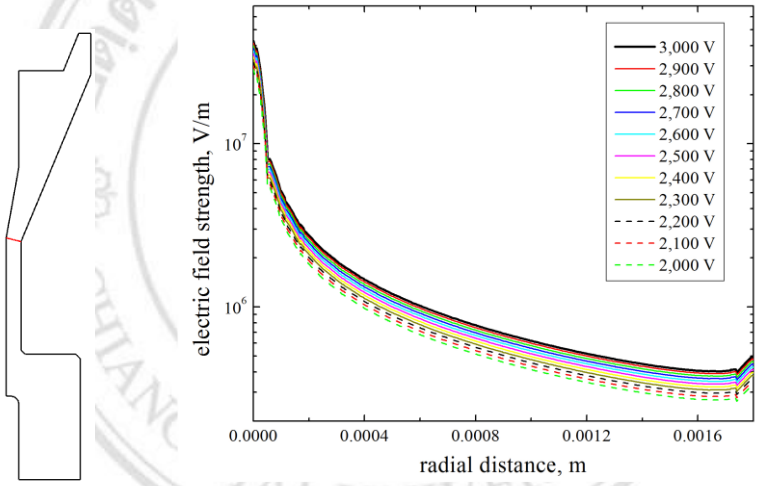

Figure 5.19 Electric field strength of needle tip when the corona voltage changes.

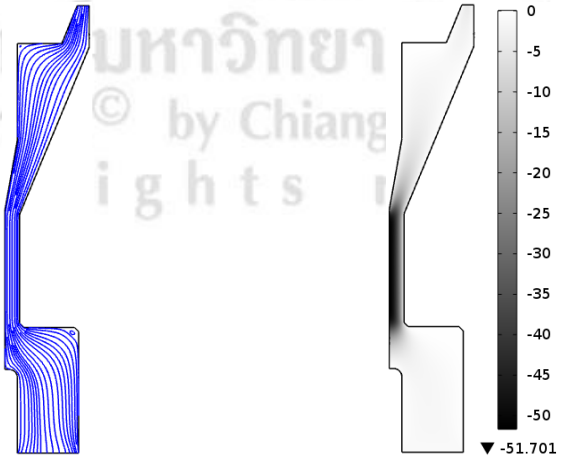

(a) Stream line of velocity field (b) Surface of velocity field (m/s)

Figure 5.20 Velocity field inside the particle charger.

Particle trajectories inside the charger were simulated. The PM of several sizes were put at the inlet of charger and pass to charging zone. All particles were set at zero charge condition. Feature of all particles was shown in Figure 5.21. The movement looked same and implied that the particle size did not have significant effect on flow for this charger. After charging process in the charging zone, the particles were charged according to size. Particle trajectories will be validated after charging zone. Number of charge electron and mass of the particles were set in Table 2.2. The ion trap zone had a varying voltage between 0 to 300 VDC. The motion of the PM is shown in Figures 5.22 to 5.25. It was shows that when the ion trap voltage was increased, the particle motion was away from the rod of the ion trap, which can be assumed that the free ion may be removed from particles in this mechanism due to higher electrical mobility than the particle (Hind 1999).

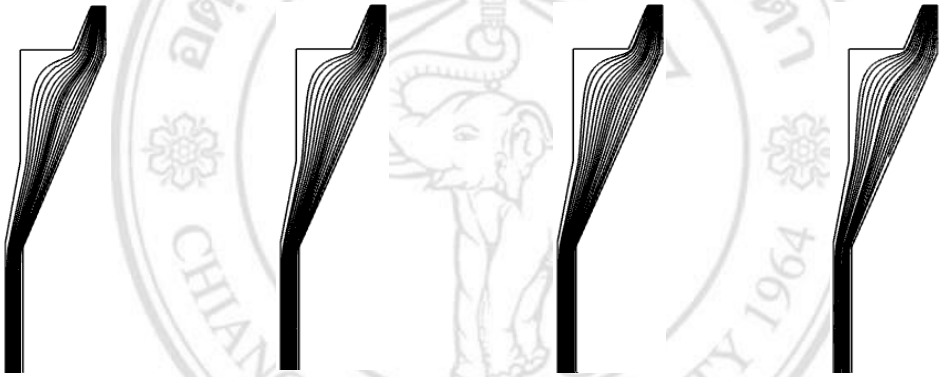

(a) PM100 (b) PM10 (c) PM2.5 (d) PM1.0

Figure 5.21 Particle trajectories without electric charge in the charging zone.

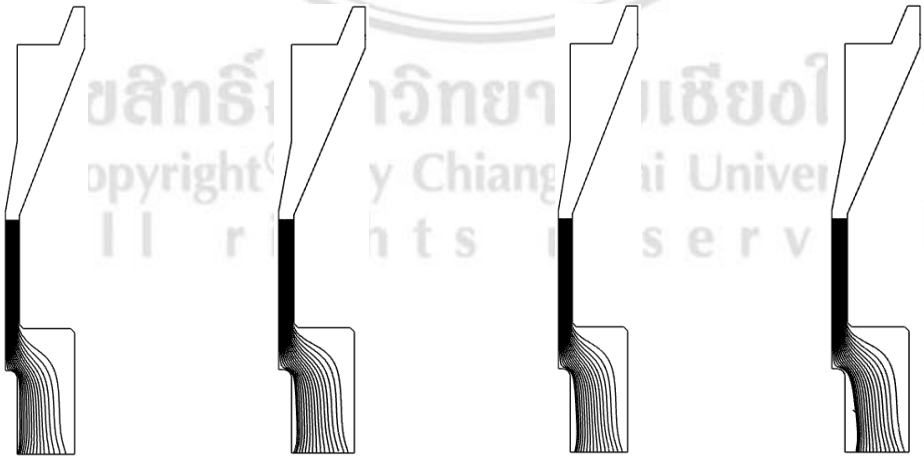

(a) 0 V (b) 50 V (c) 150 V (d) 300 V

Figure 5.22 Particle trajectories of PM100 with electric charge in ion trap zone.

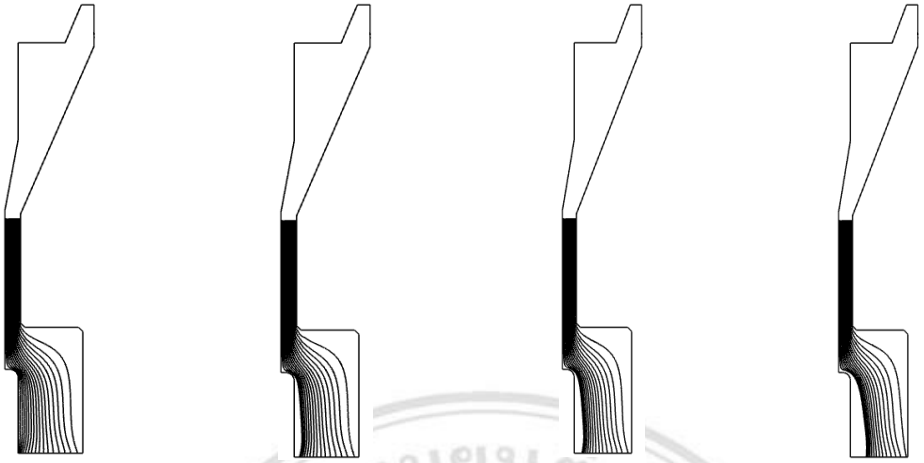

(a) 0V (b) 50V (c) 150V (d) 300V

Figure 5.23 Particle trajectories of PM10 with electric charge in ion trap zone.

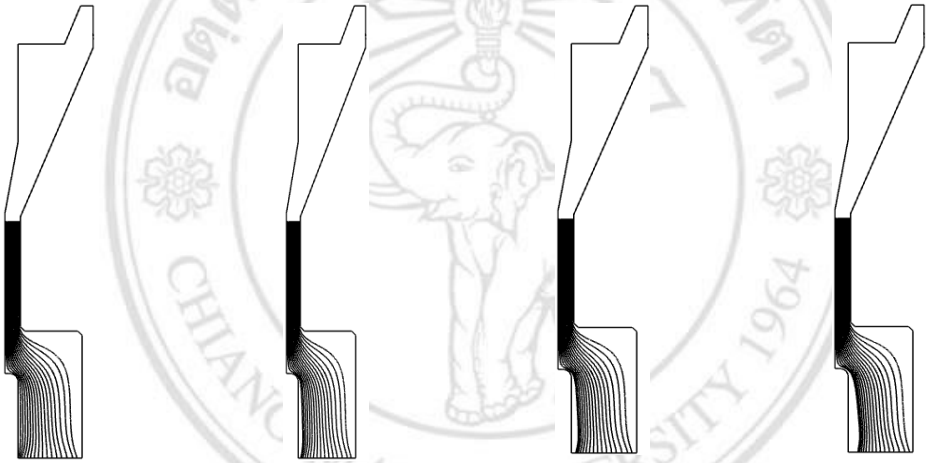

(a) 0V (b) 50V (c) 150V (d) 300V

Figure 5.24 Particle trajectories of PM2.5 with electric charge in ion trap zone.

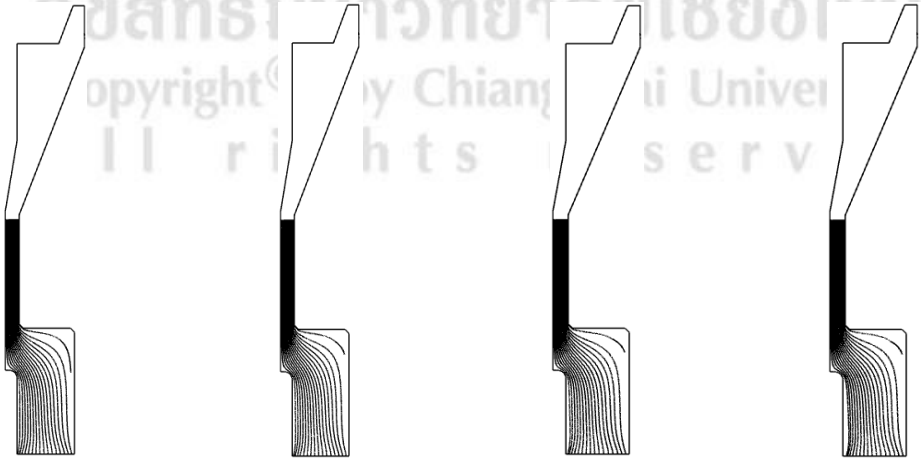

(a) 0V (b) 50V (c) 150V (d) 300V

Figure 5.25 Particle trajectories of PM1.0 with electric charge in ion trap zone.

The pressure drop was tested inside of the particle charger. This charger was designed for 15 L/min air flow rate. It should have no pressure drop at this rate. The pressure drop in each of flow rate is shown in Figure 5.26. It was found that the pressure drop was increased at more than 16 L/min in flow rate compliance with design requirements.

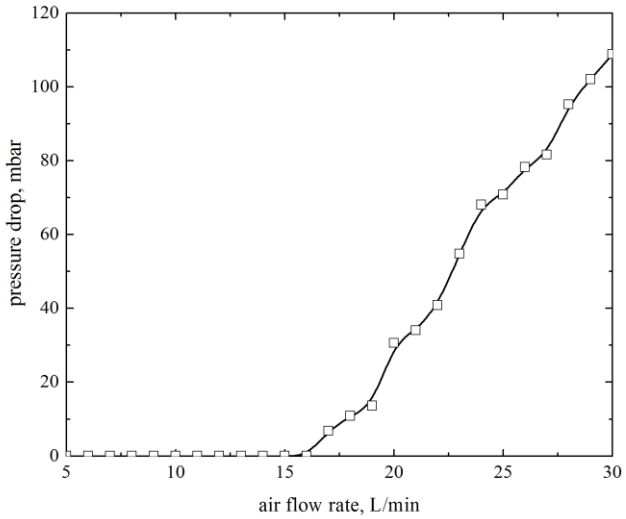

Figure 5.26 Pressure drop in the particle charger.

The high voltage power supply was used to generate 2.0 to 3.0 kV in positive and negative to the needle electrode. The outer electrode was connected to the ground. This test use the standard electrometer Keithley 6517A for measuring discharge and charging current of the charger under varying flow rate between 5 to 20 L/min. The results showed that, corona onset for positive voltage was about 2.4 kV, while the negative was about 2.2 kV as shown in Figure 5.27. The ion number concentration was about 10^{11} to 10^{16} ions/m^3 corresponding with a corona-needle ionizer of Intra and Tippayawong (2010) and the requirement of the particle charger, as shown in Section 2.4. Negative ion had more than the positive ion. The ion number concentration was increased with high voltage, as shown in Figure 5.28. Ion number product (N_it) as shown in Figure 5.29 was increased with the corona voltage. Figure 5.30 shows the ion penetration of positive and negative voltage between 5 to 20 L/min flow rate. High ion penetration was high between 75% to 80% at 15 L/min flow rate between 2.7 to 2.8 kV of positive voltage.

Influence of RH on discharge current in the charger was validated (Yawootti *et al.* 2015). The RH between 20 to 90 %RH was generated and flow into the charging zone of the charger. The applied voltage at needle electrode was between 0.5 to 2.9 kV in positive and negative voltage while setting a temperature at 27ºC. Figure 5.31 (a) shows that the discharge current was increased when the RH was high, near at 90 %RH. The negative voltage in Figure 5.31 (b) was more sensitive than positive. The discharge current was increased at about 60 %RH. When plotting in term of %RH, it was found that the RH at

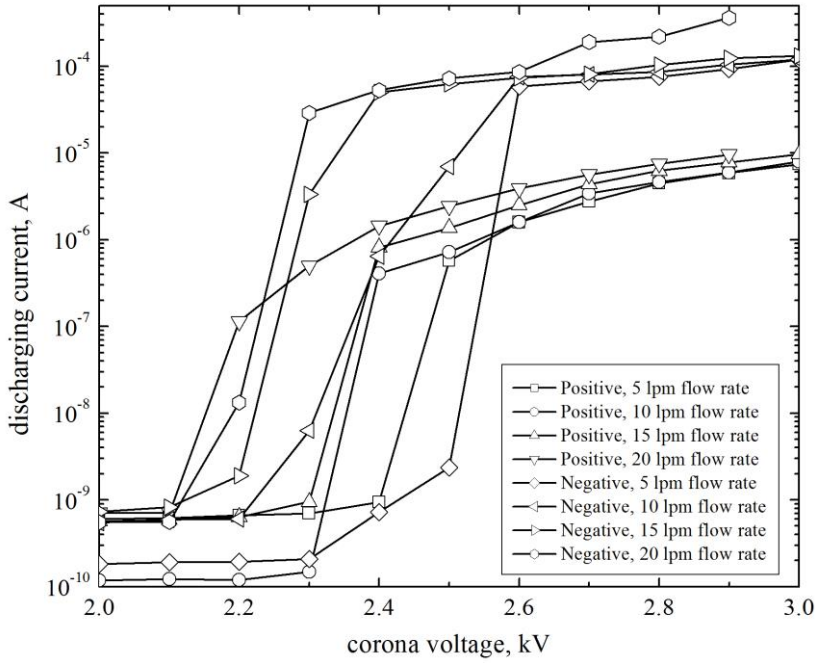

Figure 5.27 Discharge current at high voltage changes.

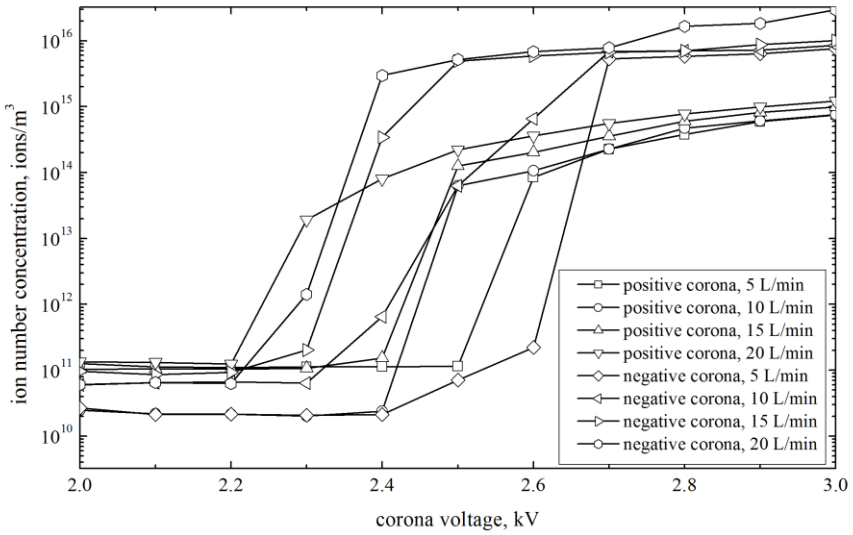

Figure 5.28 Ion number concentration at high voltage changes.

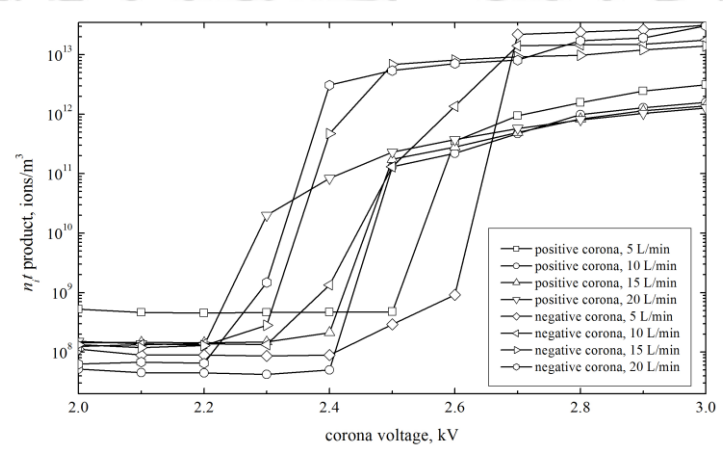

Figure 5.29 $N_i t$ product at high voltage changes.

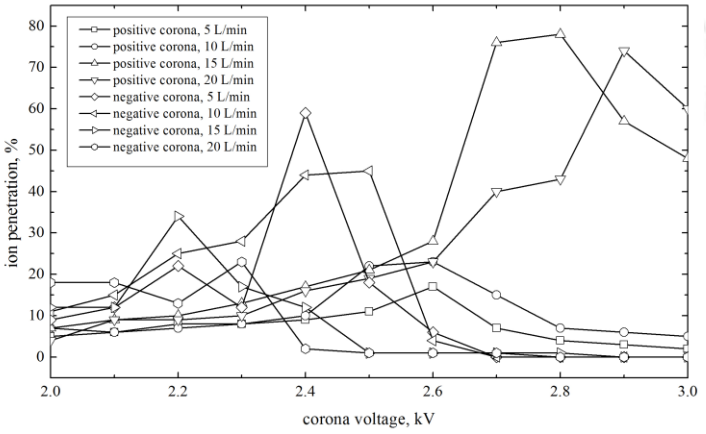

Figure 5.30 Ion penetration at high voltage changes.

90 %RH showed larger difference in a positive voltage (Figure 5.32 (a)) than negative voltage (Figure 5.32 (b)). In this thesis, a positive voltage was used to generate ions. The good condition for charging a particle must be less than 2.7 kV and 60 %RH for corona voltage and RH, respectively. When used discharge current data of 60 %RH to validate flow and corona voltage, it was found that all flows had similar discharge current, as shown in Figure 5.33.

Normally, the corona onset and breakdown voltage of positive type are found at low voltage than negative type. In case of unstable temperature, the corona onset and breakdown voltage happened at low voltage. This relation is found inside the charger. When the charger temperature was increased, it was found that the discharge current of the positive breakdown voltage had many changes about 45 ^{o}C, as shown in Figure 5.34, corresponding with negative type. When changing the corona voltage at different temperature, it was found that the discharge current were increased with temperature. The positive discharge current was high at 30^{o}C (Figure 5.35 (a)), while negative discharge current changes at 50 ^{o}C (Figure 5.35 (b)). Figure 5.36 (a) shows increasing discharge current from corona high voltage and temperature. It was found that the positive about 2.6 kV and under 40 ^{o}C was less than the high conditions. Figure 5.36 (b) shows that temperature between 10 to 50 ^{o}C had less difference for discharge current under negative corona between 2.0 to 2.4 kV.

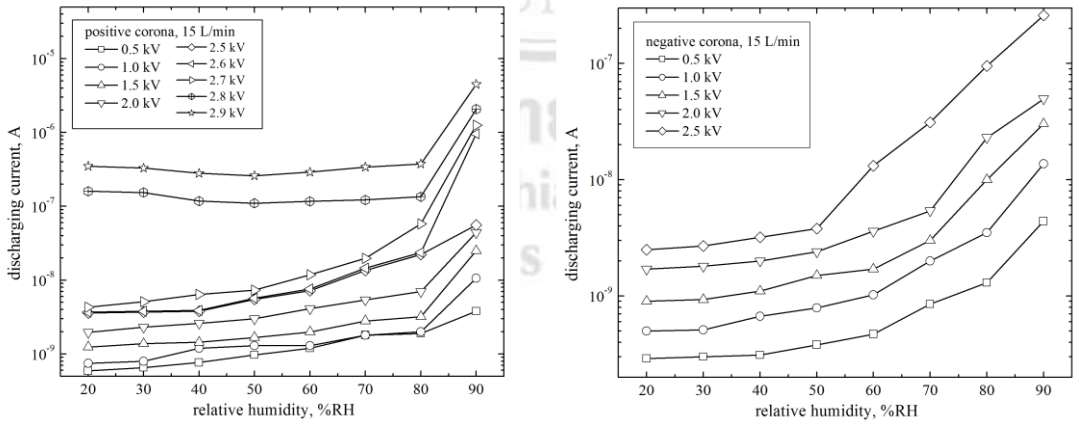

(a) Positive corona (b) Negative corona

Figure 5.31 Discharge current when the RH changes.

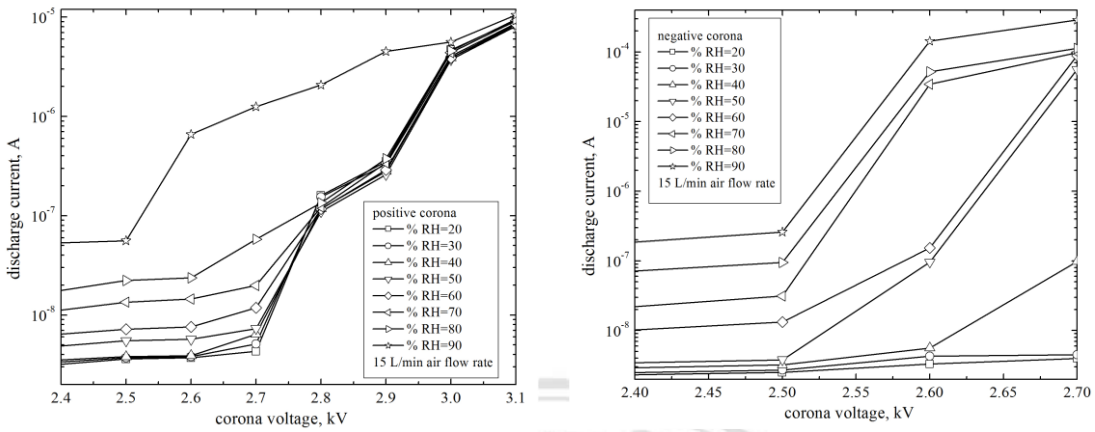

(a) Positive corona (b) Negative corona

Figure 5.32 Discharge current when the corona voltage changes.

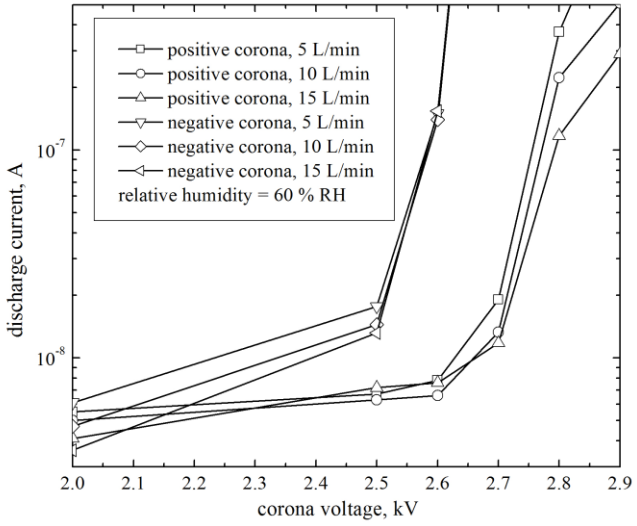

Figure 5.33 Discharge current at 60%RH when the corona voltage changes.

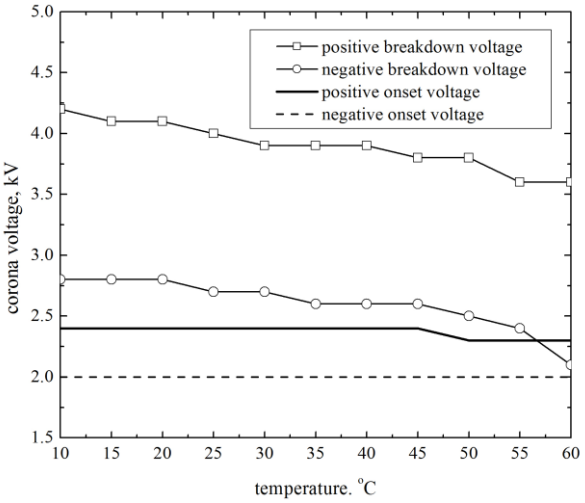

Figure 5.34 Corona onset and breakdown voltage.

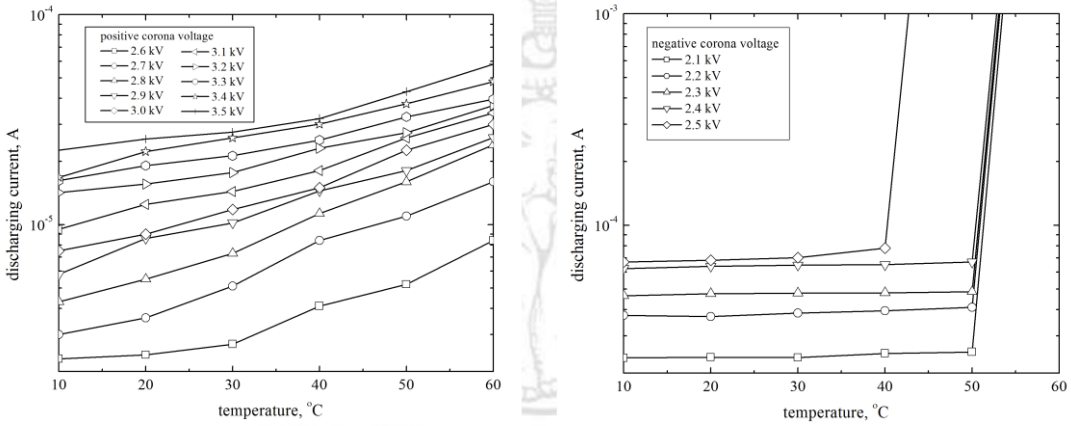

(a) Positive corona (b) Negative corona

Figure 5.35 Discharge current when the temperature changes.

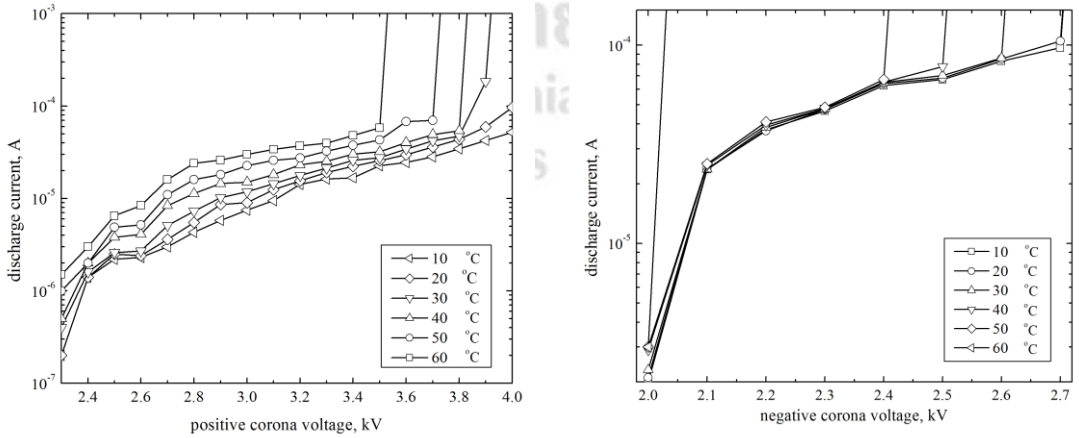

(a) Positive corona (b) Negative corona

Figure 5.36 Discharge current when the corona voltage changes.

5.3 Characteristic of Particle Size Classification, Faraday Cup and Cage

Figure 5.37 shows collection efficiency of particles in PM10, PM2.5, and PM1.0 at 5 L/min flow rate by analytical analysis. This validation was considered for 100 nm to 100 μm in particle diameter. The cutoff diameters of the impactors for PM10, PM2.5, and PM1.0 were 9.98×10^{-6}, 2.47×10^{-6} and 0.92×10^{-6} m, respectively (Intra *et al.* 2012). The particle trajectories were validated inside the impactor. Particles smaller than the cutoff diameter flow to the outlet, while the bigger particles were collected in the impaction plate. The particles equal to the cutoff diameter had 50 % for passing, according to the impaction theory.

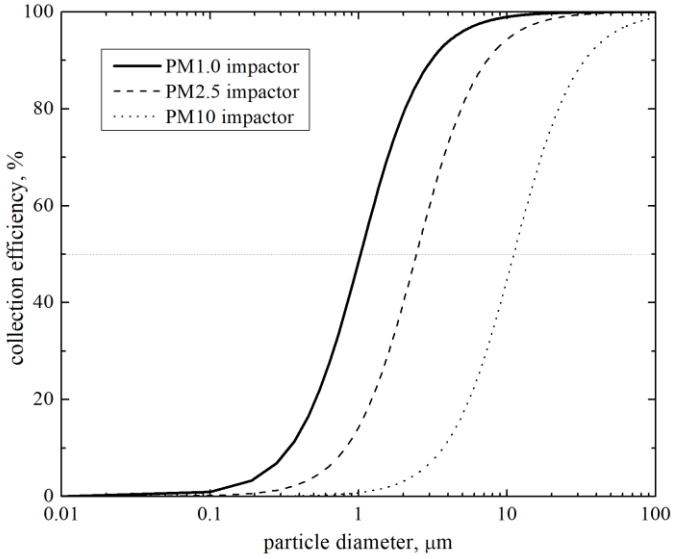

Figure 5.37 Collecting efficiency from analytical analysis at 5 L/min air flow rate.

The nozzle tip axial was used to find the average velocity of PM10, PM2.5, and PM1.0 impactor. This value was used to find the minimum mesh that gives stability. The average velocity was stable at about 40,000 mesh domains, as shown in Figure 5.38 (a) (b) and (c), respectively. In this study, mesh parameters were set in domain of geometric entity level, which was triangular type and had 4.92×10^4, 4.49×10^4 and 4.86×10^4 mesh domains for PM10, PM2.5, and PM1.0 impactor, as shown in Figure 5.39 (a) (b) and (c), respectively. Figure 5.40 (a) (b) and (c) show the arrow direction of air flow inside of PM10 PM2.5, and PM1.0, respectively. The air samples flowed from the nozzle and passed to the impaction plate, then to the side exit. Concentration of flow were high at nozzle area and diffuse to the outer area. When 2D cut line from the nozzle jet was used

to the impaction plate, it was found that the flow velocity decrease from the nozzle jet position to the impaction plate, shown in Figure 5.41. When monodisperse particles were put in over, under and equal the cutoff diameter (d_{50}) of each impactor, it was found that the over size of d_{50} had the particle trajectory impact of the impactor plate, while the under size and some of equal size of d50 in diameter can pass through to the outlet as shown in Figures 5.42 to 5.44 for PM10, PM2.5, and PM1.0 impactor, respectively.

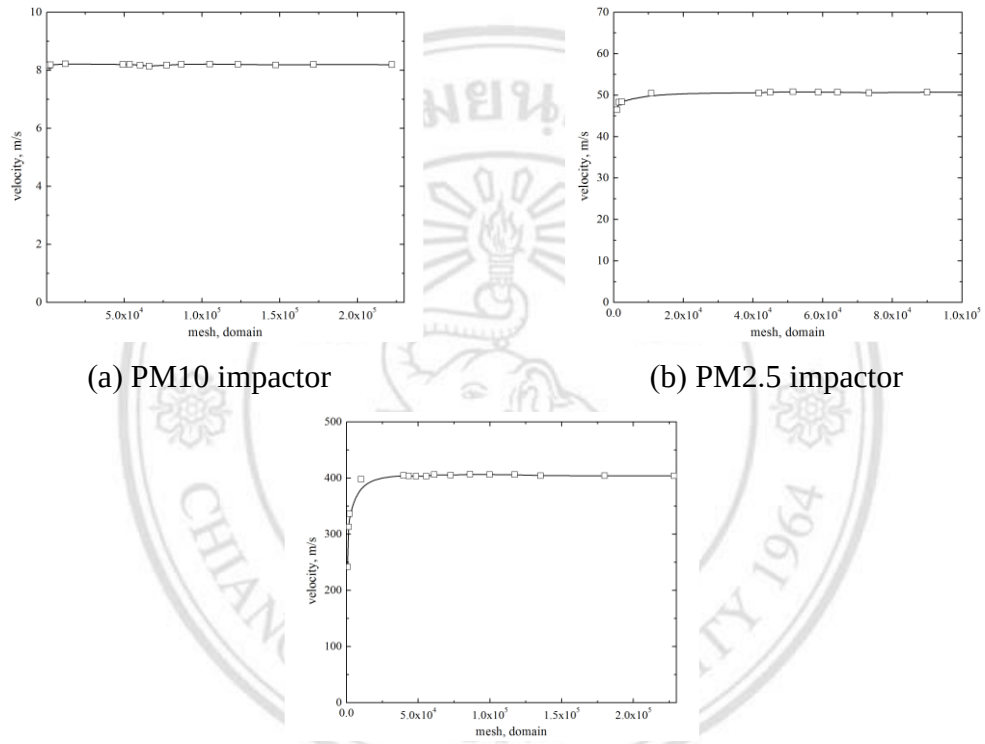

(a) PM10 impactor (b) PM2.5 impactor

(d) PM1.0 impactor

Figure 5.38 Velocity field average when mesh domain changes.

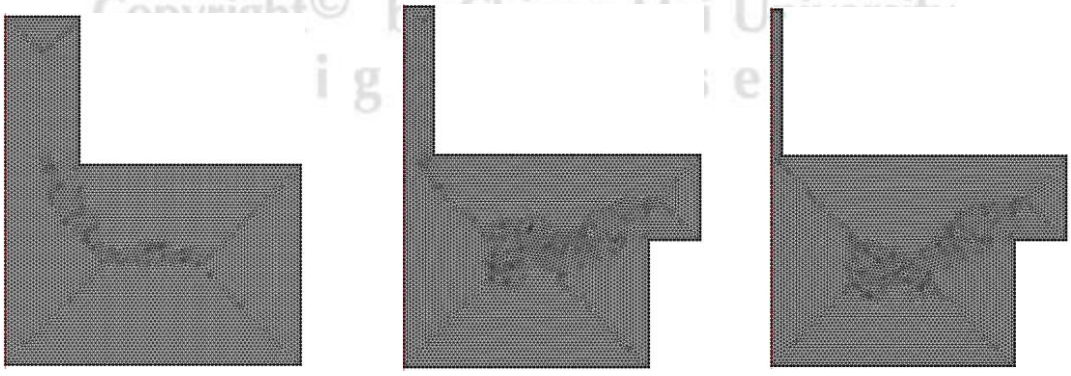

(a) PM10 impactor (b) PM2.5 impactor (c) PM1.0 impactor

Figure 5.39 Mesh domains of the particle size selector.

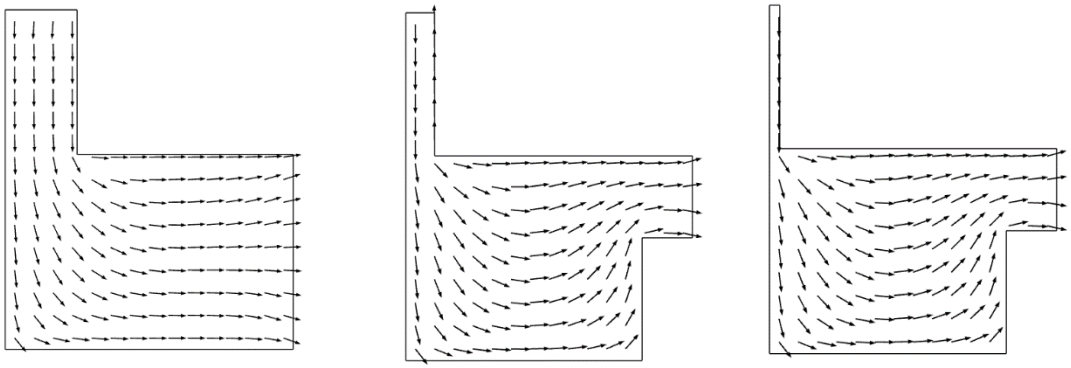

(a) PM10 impactor (b) PM2.5 impactor (c) PM1.0 impactor

Figure 5.40 Arrow direction of velocity field in the particle impactors.

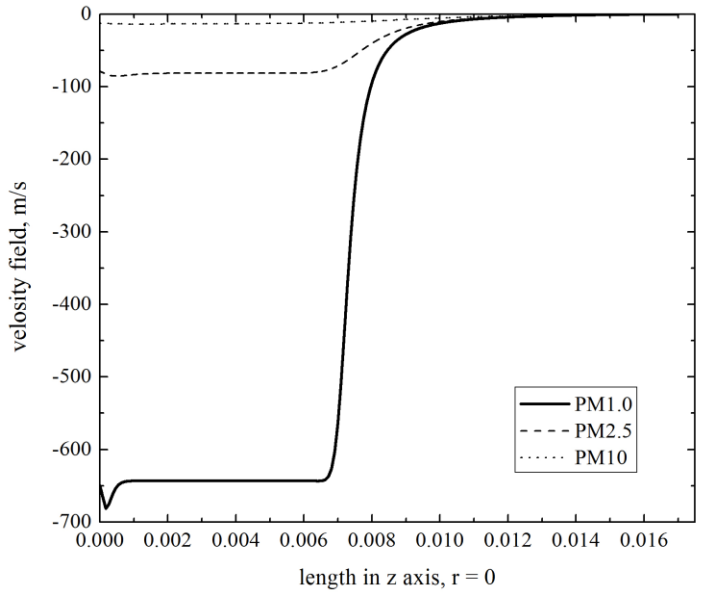

Figure 5.41 Velocity field allows z axis (r = 0).

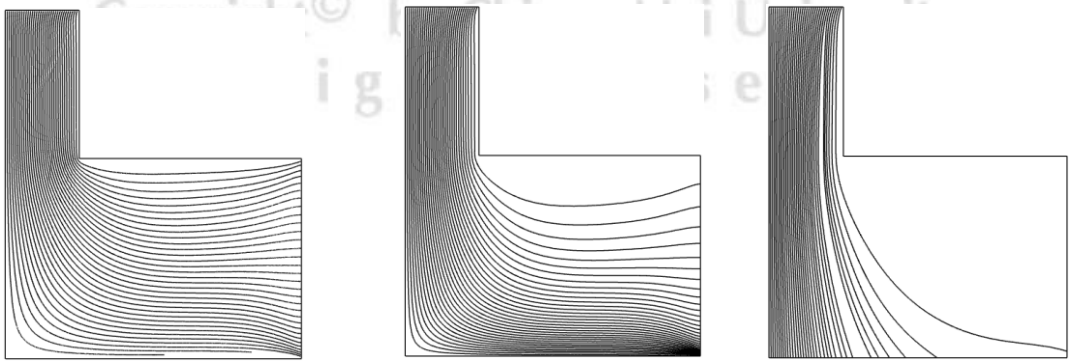

(a) 2.5×10^{-6} m dia. (b) 10×10^{-6} m dia. (c) 100×10^{-6} m dia.

Figure 5.42 Particle trajectories in the PM10 impactor.

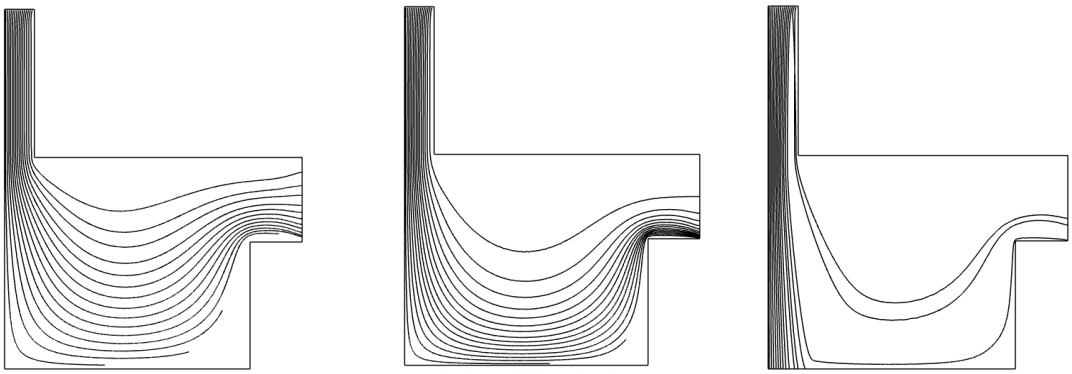

(a) 1.0×10^{-6} m dia. (b) 2.5×10^{-6} m dia. (c) 10×10^{-6} m dia.

Figure 5.43 Particle trajectories in the PM2.5 impactor.

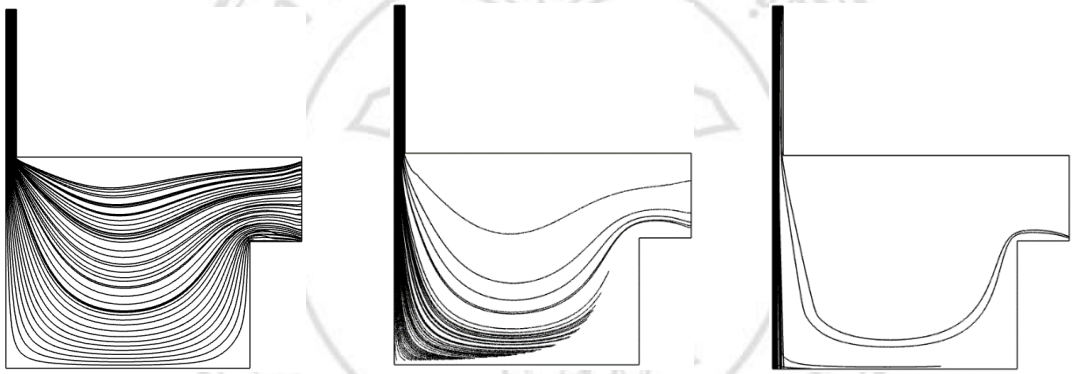

(a) Massless particles (b) 1.0×10^{-6} m dia. (c) 2.5×10^{-6} m dia.

Figure 5.44 Particle trajectories in the PM1.0 impactor.

The average velocity at the Faraday cup surface of PM10, PM2.5, and PM1.0 detectors in each domains number are shown in Figure 5.45. It was found that the results were stable at more than about 300,000 mesh domain. Mesh parameters in this study were set in extra fine domain and extremely fine in all boundaries at a geometric entry level which was triangular type and fluid dynamic condition. The complete mesh had about 4.89×10^5, 4.28×10^5 and 4.26×10^5 for PM10, PM2.5, and PM1.0 detectors, as shown in Figure 5.46 part (a) to (c), respectively. The velocity arrows inside the Faraday cage of PM10, PM2.5, and PM1.0 were flowing from the inlet to the impaction plate and through the Faraday cup, as shown in Figure 5.47 part (a) to (c), respectively. It was turbulence flow at the side and base of a cup. The nozzle jets had a maximum flow at 17.75, 112.08 and 868.67 m/s for PM10, PM2.5, and PM1.0 detectors. Next, the PM was released into each detector for validating the flow field. Figure 5.48 shows the particles spread evenly on a Faraday cup surface. The velocity field in of the Faraday cup's surface as shown in

Figure 5.49 (a) were compared. It was found that maximum flow was about 1 m/s at the center and decreased at around follow r-axial distance, as shown in Figure 5.49 (b). This flow characteristic made most particle collected in the center filter region.

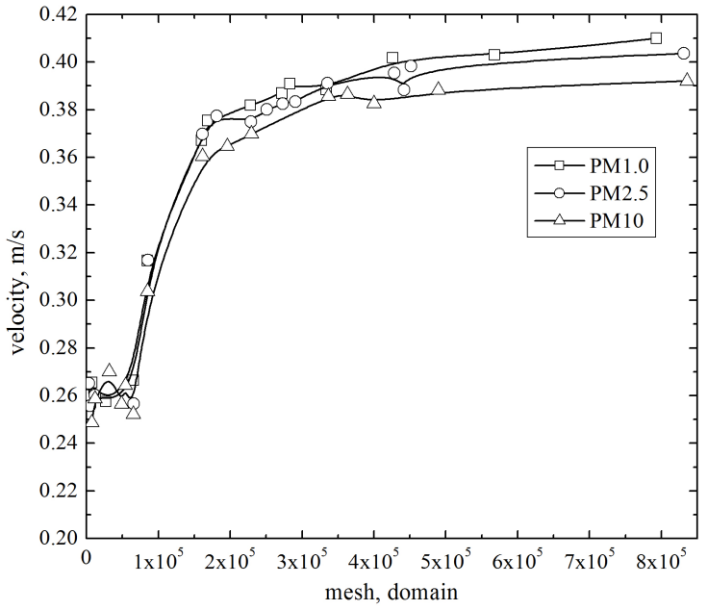

Figure 5.45 Velocity average in each of domains number.

The SMPS and CPC were validated to find the particle loss in the Faraday cage since the inlet to outlet. The TOPAS ATM226 atomizer was used to generate the water spray between 10 to 500 nm in diameter. Figure 5. 50 shows the NaCl aerosols concentration between inlet and outlet at before and after the HEPA filter in the Faraday cage. It was found that the NaCl aerosols loss was less than 10 % and the HEPA filter had high efficiency for filtering the fine particle.

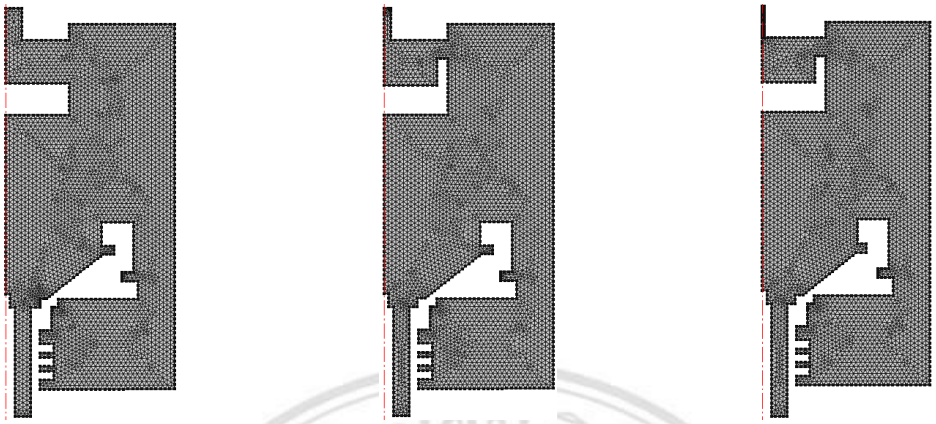

(a) PM10 (b) PM2.5 (c) PM1.0

Figure 5.46 Mesh domains of the Faraday cage.

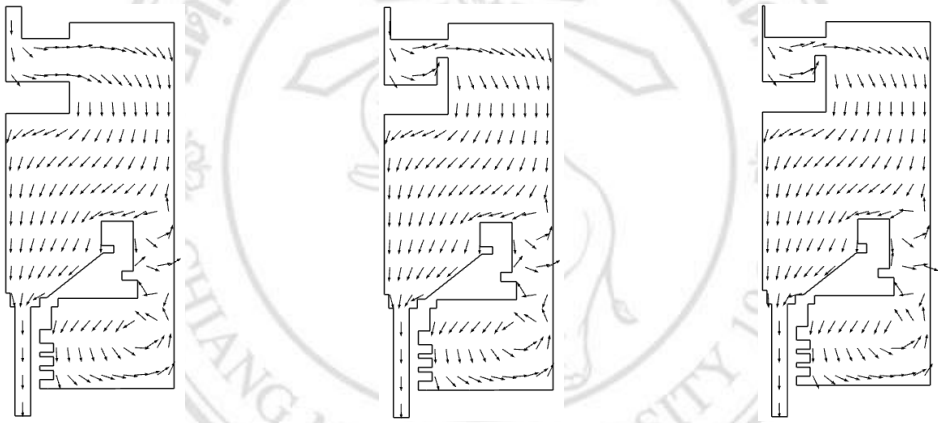

(a) PM10 (b) PM2.5 (c) PM1.0

Figure 5.47 Aero direction of velocity field in the Faraday cage.

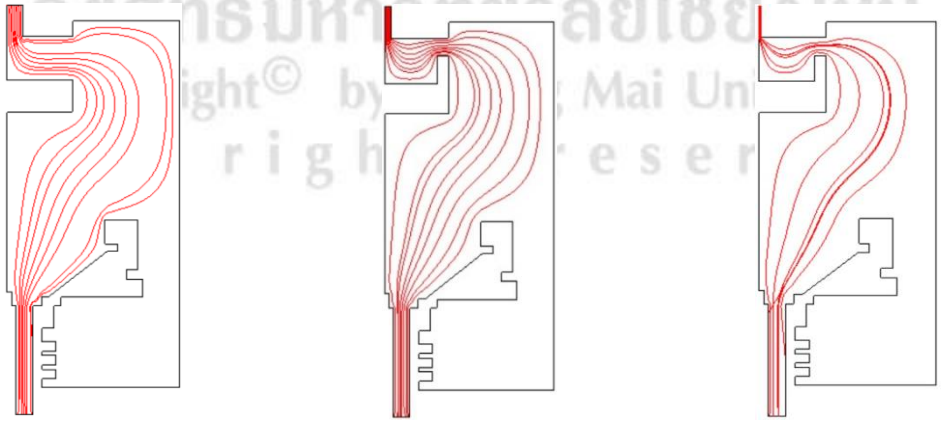

(a) PM10 (b) PM2.5 (c) PM1.0

Figure 5.48 Particles tracing inside the particle detector.

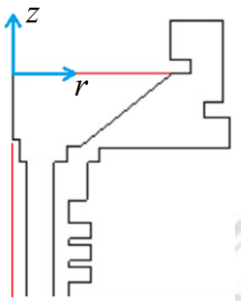

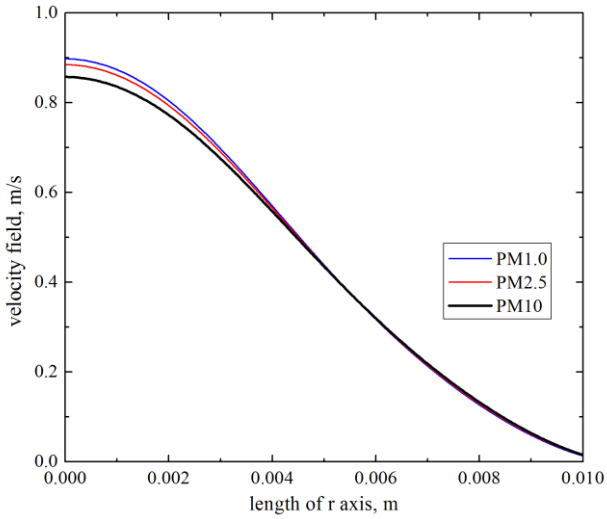

(a) Axial cut line for validation. (b) The velocity flow at r-axis changes.

Figure 5.49 Comparison of flow velocity at the surface Faraday cup.

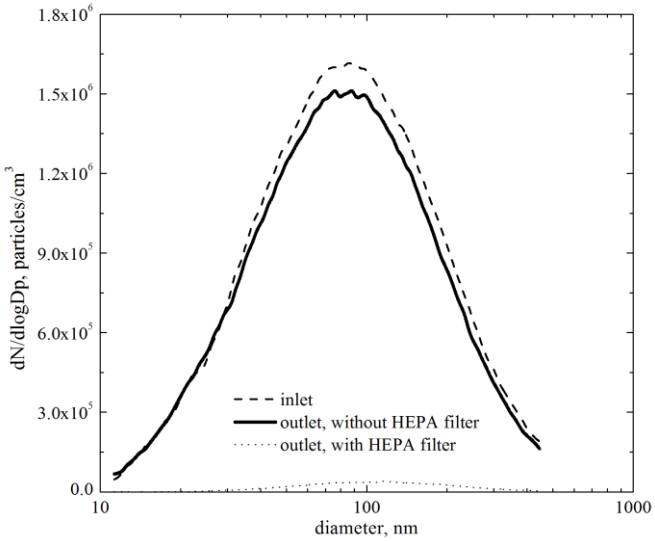

Figure 5.50 Nano particle loss in the Faraday cage.

The carbon tape was attached to surface of the impaction plate and Faraday cup to sample particles for validation by the scanning electron microscope (SEM). TOPAS ATM226 was used to generate the NaCl aerosols in a closed room 8 m^3 in volume for this test. A feature of the poly disperse aerosol on the impaction plate of PM10, PM2.5, and PM1.0 is shown in part (a) of Figures 5.51 to 5.53, respectively. Aerosol less than 10, 2.5, and 1.0 μm in diameter can pass through to the Faraday cup, as shown in part (b) of Figures 5.51 to 5.53, respectively (Some NaCl sample in Figure 5.52 were melted on the surface of the sample filter).

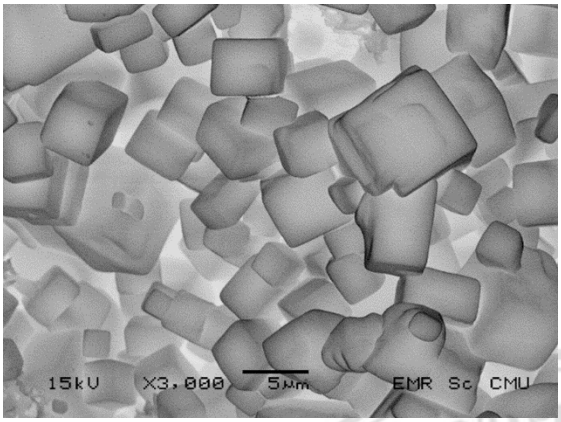

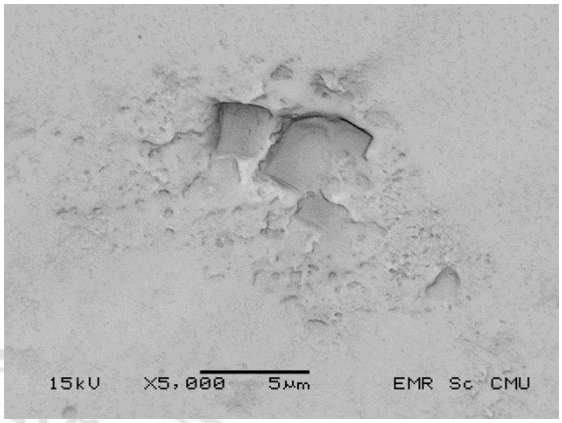

(a) The sample on the PM10 impactor (b) The sample after the PM10 impactor

Figure 5.51 Morphology photo of the NaCl in the PM10 impactor.

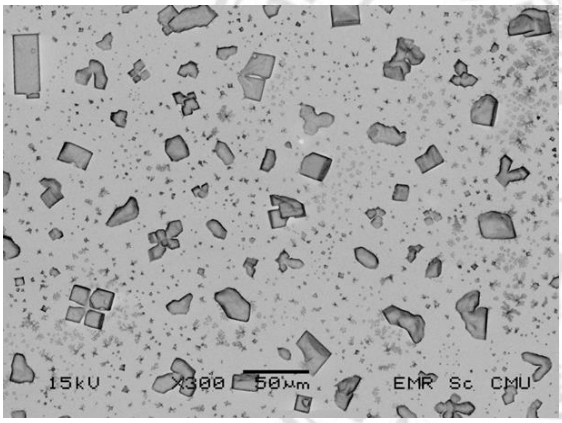

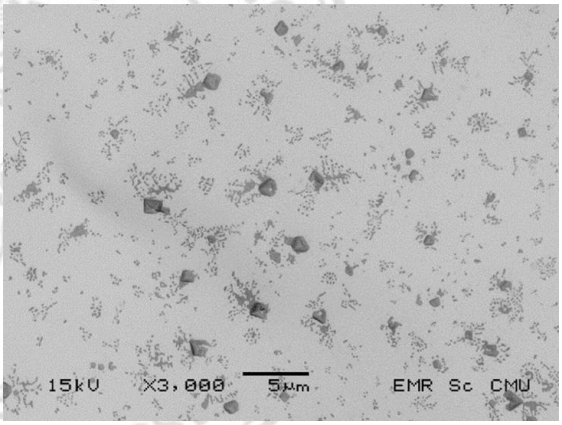

(a) The sample on the PM2.5 impactor (b) The sample after the PM2.5 impactor

Figure 5.52 Morphology photo of the NaCl in the PM2.5 impactor.

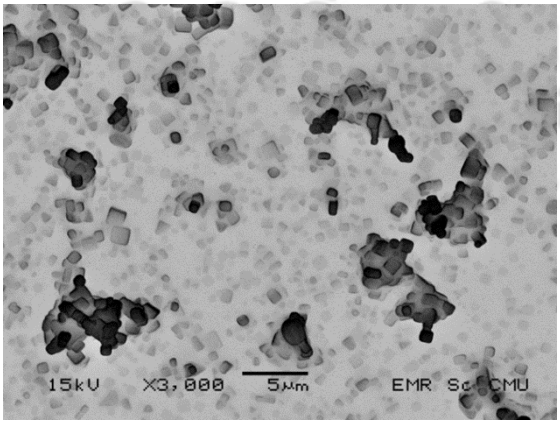

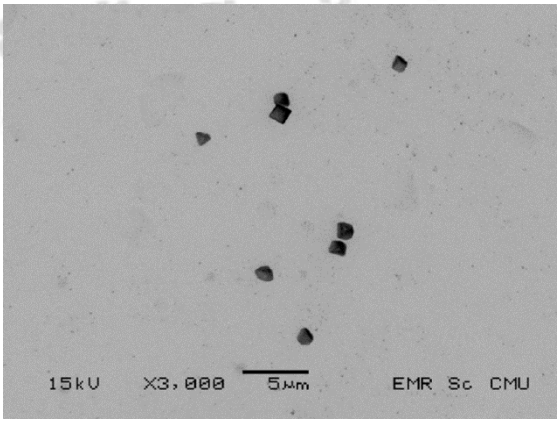

(a) The sample on the PM1.0 impactor (b) The sample after the PM1.0 impactor

Figure 5.53 Morphology photo of the NaCl in the PM1.0 impactor.

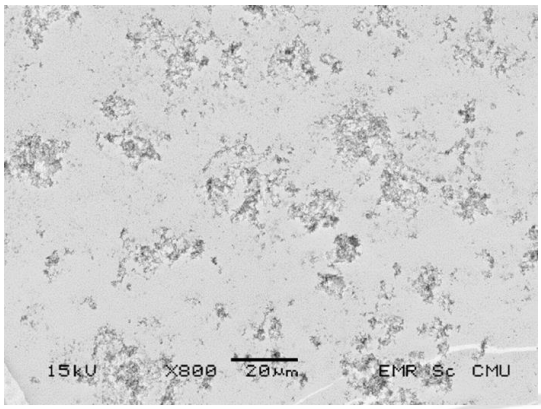

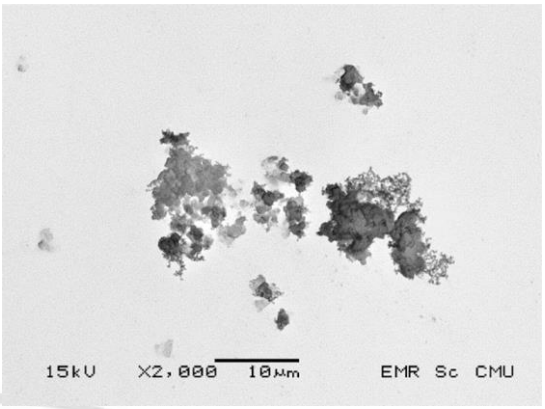

(a) The sample on the impactor (b) The sample after the impactor

Figure 5.54 Morphology photo of the combustion particle in the PM10 impactor.

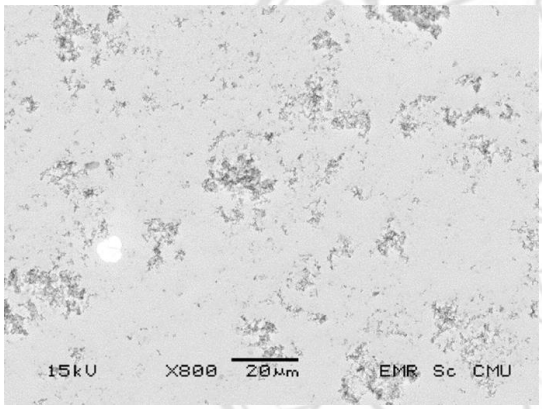

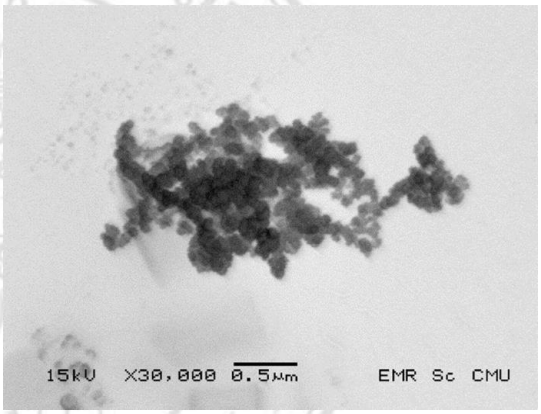

(a) The sample on the impactor (b) The sample after the impactor

Figure 5.55 Morphology photo of the combustion particle in the PM2.5 impactor.

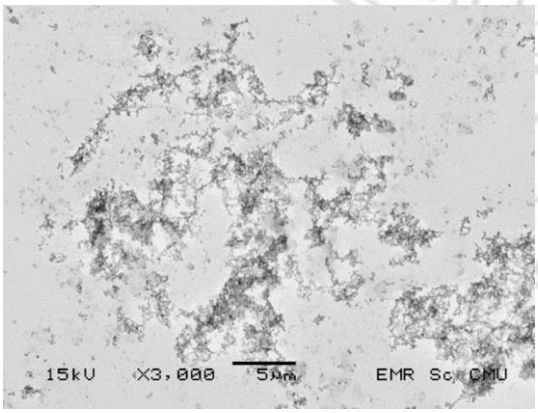

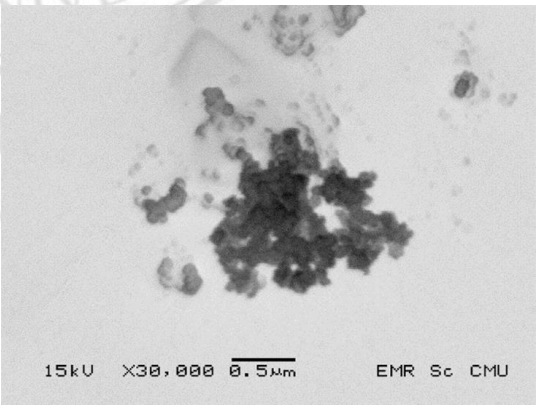

(a) The sample on the PM1.0 impactor (b) The sample after the PM1.0 impactor

Figure 5.56 Morphology photo of the combustion particle in the PM1.0 impactor.

Figures 5.54 to 5.56 (a) show a feature of combustion aerosol on the impaction plate of PM10, PM2.5, and PM1.0, respectively. The aerosol particles that flow through a Faraday cup of PM10, PM2.5, and PM1.0 as shown in part (b) of Figures 5.54 to 5.56,

respectively. Both aerosol particles from the NaCl and combustion passed to Faraday and had size according to the cut point diameter of each impactor size. This result can confirm that prototypes of the particle impactor can classify size of the PM10, PM2.5, and PM1.0.

Laboratory test used high concentration samples from the aerosol generator in closed room 8 m^3 in volume. But, field test had low concentration particle. So long time was needed to validate about 24 h or more. The samples from ambient aerosol on the impaction plate are shown in part (a) of Figures 5.57 to 5.59. Sampling aerosol on a Faraday cup was difficult to find on carbon tape. Most of the particles may flow around the carbon tape, not stick to carbon surface. However, there were some particles still stick on the carbon tape, shown in part (b) of Figures 5.57 to 5.59 for PM10, PM2.5, and PM1.0 impactor, respectively.

Figure 5.60 (a) shows features of a HEPA filter on Faraday cup when sampling PM for more than 700 h continuously, while (b) shows some of PM samples in the HEPA filter on a thread.

5.4 Characteristic of Electrometer Circuit

Electrometer circuit in this thesis was a basic inverting circuit that used the CMOS LMC6032 and resistor 500 GΩ for amplifier and feedback resistor, respectively. This circuit was a high gain amplified and can amplify the ultra-low current in Femto Amp levels (10^{-15}). From Eqs. (2.58), the input current between 20 fA to 10 pA was used to calculate the output voltage (analytical) from 0.01 to 5 V. While numerical simulation of to the PSpice software (student version 9.23) was used to compute the numerical output voltage (V_{Onum}) and compare with theory (V_{OT}). LMC6032 electrometer in this test had 5 circuits (V_{O1} to V_{O5}) and can compare output voltage as shown in Table 5.1. Figure 5.61 shows a simulation circuit of current sources and LMC6032 op-amp circuit for this numerical calculation. After that, the output voltage from LMC6032 circuits was measured by Keithley 6517A electrometer. Ultra-low current source as used (shown in Figure 4.38), which can convert 0.01 to 5 VDC voltage from Keithley 6517A power

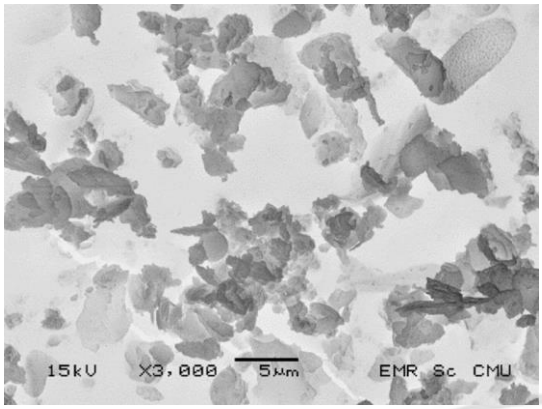

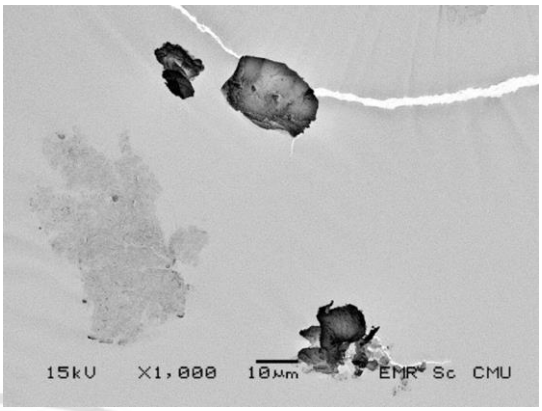

(a) The sample on the PM10 impactor (b) The sample after the PM10 impactor

Figure 5.57 Morphology photo of the airborne particle in the PM10 impactor.

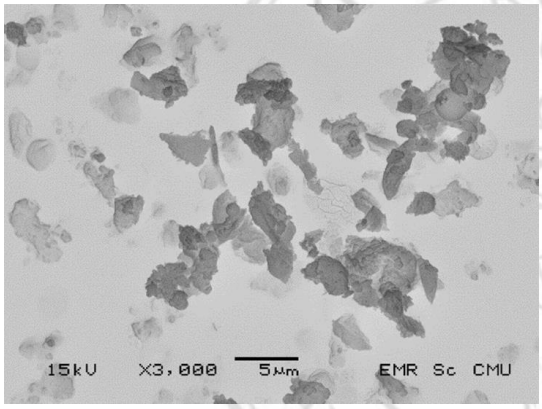

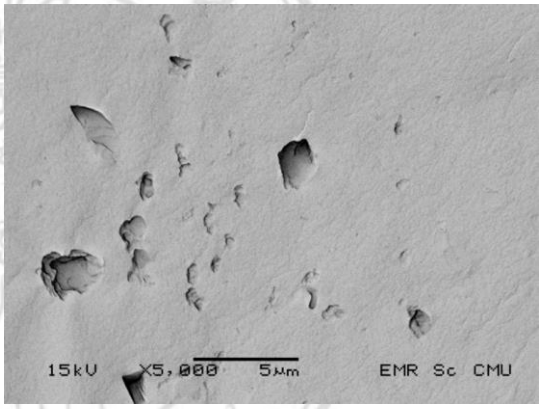

(a) The sample on the PM2.5 impactor (b) The sample after the PM2.5 impactor

Figure 5.58 Morphology photo of the airborne particle in the PM2.5 impactor.

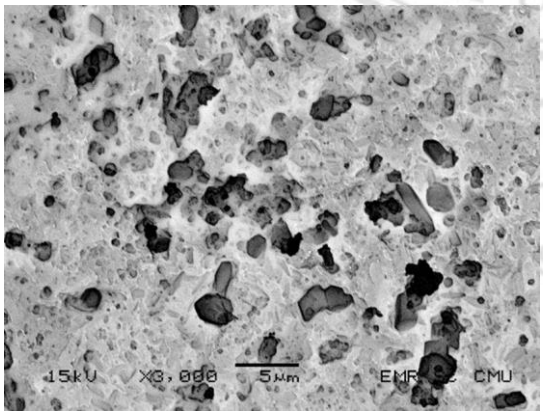

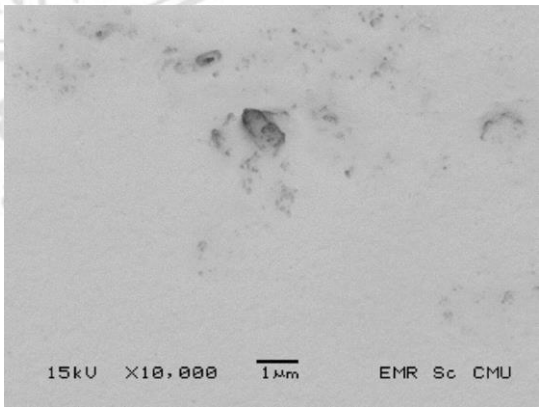

(a) The sample on the PM1.0 impactor (b) The sample after the PM1.0 impactor

Figure 5.59 Morphology photo of the airborne particle in the PM1.0 impactor.

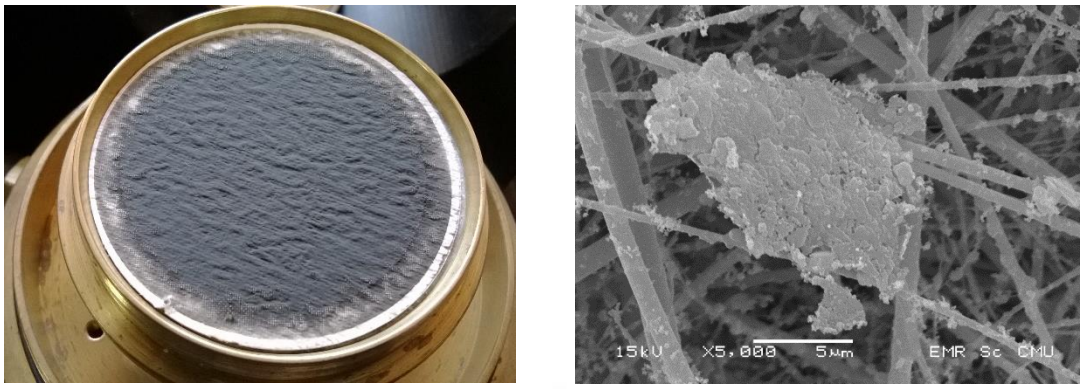

(a) HEPA filter in Faraday cup (b) Aerosol in a thread

Figure 5.60 Aerosol particle on the HEPA filter.

supply to 20 fA to 10 pA currents. Figure 5.62 shows a comparison of the low range between 0 to 2 pA in input current and 0 to 1 V in output voltage of numerical simulation and LMC6032 circuits, while Figure 5.63 shows a comparison of the high range between 2 to 10 pA input current and 1 to 5 V output voltage from numerical simulation and LMC6032 circuits. Both ranges are shown in Figure 5.64 and have accuracy between 0.488 to 5.55% and 0.11 to 7.0% (these number are the error values) for numerical simulation and 5 circuits of LMC6032, respectively. The measuring range of particle number concentration can be calculated from Eqs. (2.56), and the total charge from Table 2.7. There were found to be between 6.747×10^{5} to 3.374×10^{8}, 9.653×10^{6} to 4.825×10^{9} and 5.159×10^{7} to 2.58×10^{10} particles/m^3 of PM10, PM2.5, and PM1.0, respectively.

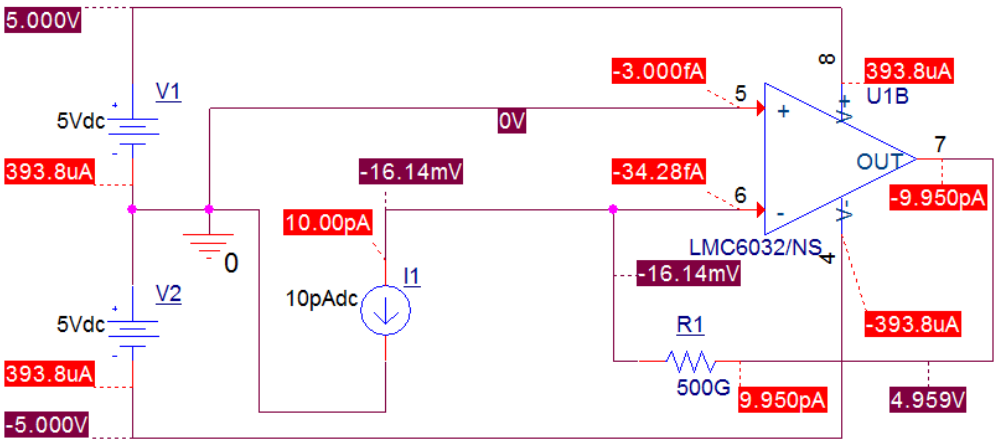

Figure 5.61 Simulation circuit of current source and LMC6032 op-amp circuit.

Table 5.1 Output voltage of an electrometer.

I_{in} (pA)	$V_{OT}=I_{in}*R_{cal}$	V_{Onum}	V_{O1}	V_{O2}	V_{O3}	V_{O4}	V_{O5}
0.02	0.01	0.0102	0.0103	0.0107	0.0106	0.0104	0.0101
0.10	0.05	0.0517	0.0512	0.0504	0.0516	0.0516	0.0511
0.20	0.1	0.103	0.0981	0.103	0.102	0.102	0.103
0.40	0.2	0.2111	0.205	0.207	0.213	0.205	0.21
0.60	0.3	0.3115	0.297	0.311	0.316	0.317	0.295
0.80	0.4	0.4215	0.396	0.416	0.412	0.408	0.393
1.00	0.5	0.5215	0.494	0.517	0.513	0.498	0.498
1.20	0.6	0.6215	0.592	0.601	0.617	0.602	0.596
1.40	0.7	0.7215	0.694	0.711	0.724	0.716	0.684
1.60	0.8	0.8215	0.789	0.815	0.814	0.813	0.789
1.80	0.9	0.9215	0.901	0.92	0.928	0.915	0.889
2.00	1.0	1.022	0.995	1.04	1.04	1.03	0.983
3.00	1.5	1.522	1.51	1.56	1.52	1.52	1.46
4.00	2.0	2.022	2.07	2.08	2.06	2.02	1.96
5.00	2.5	2.522	2.51	2.59	2.58	2.57	2.44
6.00	3.0	3.022	3.03	3.04	3.04	3.07	2.95
7.00	3.5	3.522	3.51	3.65	3.57	3.55	3.45
8.00	4.0	4.022	4.06	4.17	4.05	4.03	3.92
9.00	4.5	4.522	4.56	4.63	4.57	4.55	4.42
10.00	5.0	4.959	4.87	4.86	4.87	4.85	4.88

5.5 Characteristic of Vacuum Pump

The vacuum pump was tested by finding relationship between operating voltage, current and flow rate. Figure 5.65 shows the operation at no load condition of vacuum pump. It can operate at 5 VDC with 60 L/min maximum flow rate, while, the operating current was between 3.0 to 5.0 A. The vacuum pump was the appliances that use the most energy in system and it was set at 12 VDC voltage which the continuous PM monitoring in this thesis can operate more than 12 h for a 70 Ah battery.

5.6 Characteristic of High Voltage Power Supply

The Spellman power supply model 0.1P0.5/12 and MM0.1P1.5/12 were tested to find electrical characteristic. Figure 5.66 shows the relationship between input and output voltage of Spellman model MM0.1P0.5/12. This model can generate the output voltage since 0.5 V input. The ratio of the output and input voltage showed high linearity. Figure 5.67 shows the relationship of the input and output voltage of Spellman model MM0.1P1.5/12.

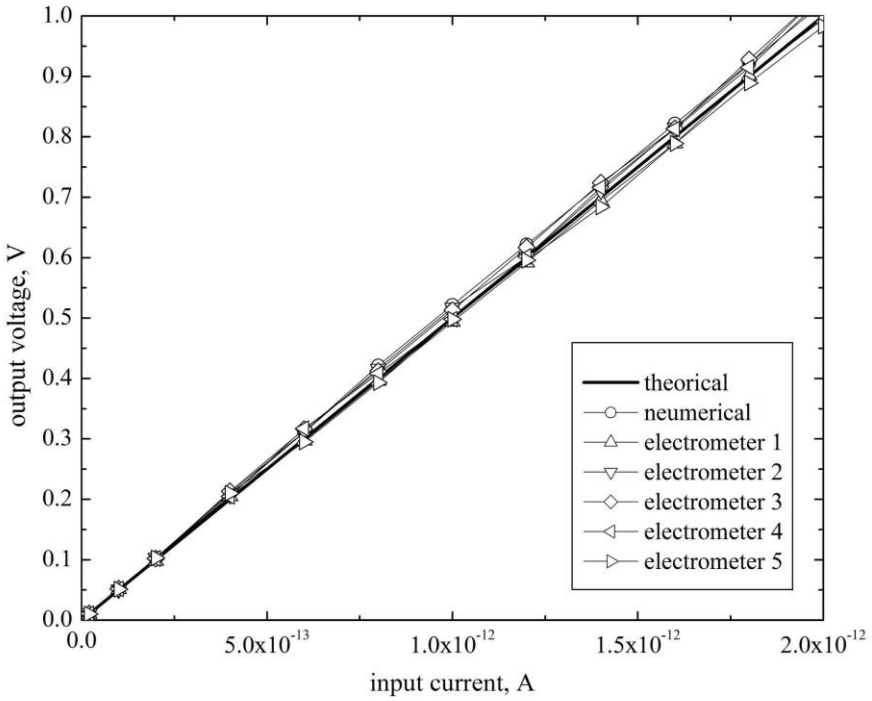

Figure 5.62 Comparison between 20 to 2,000 fA (input) and 0.001 to 1 V (output).

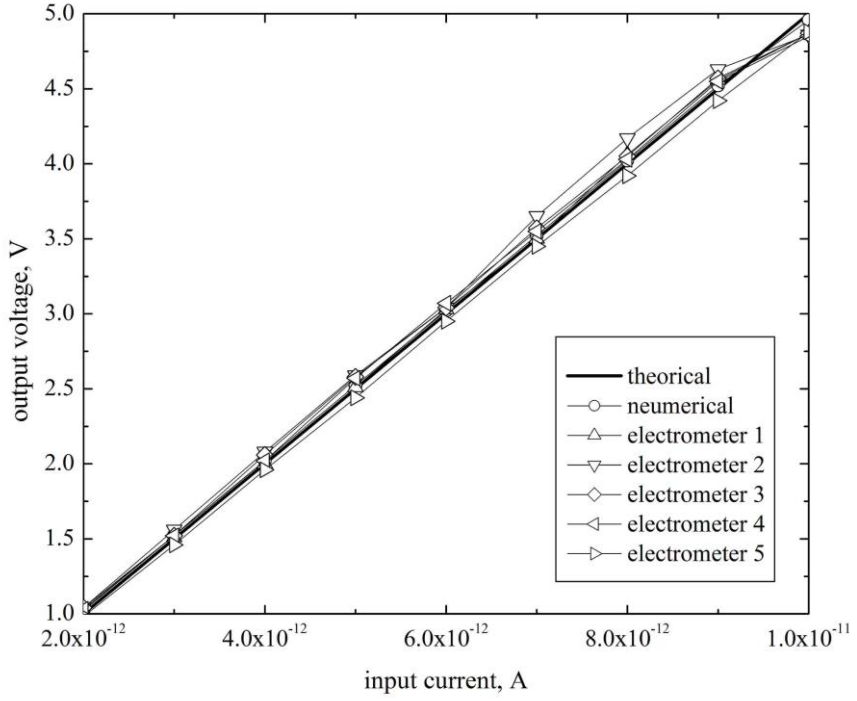

Figure 5.63 Comparison between 2 to 10 pA (input) and 1 to 5 V (output).

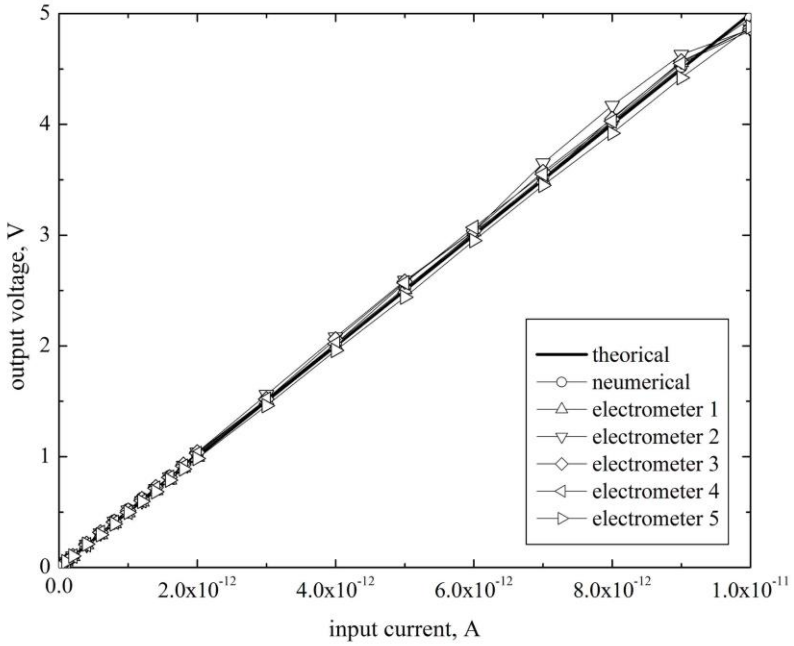

Figure 5.64 Comparison between 20 fA to 10 pA (input) and 0.01 to 5 V (output).

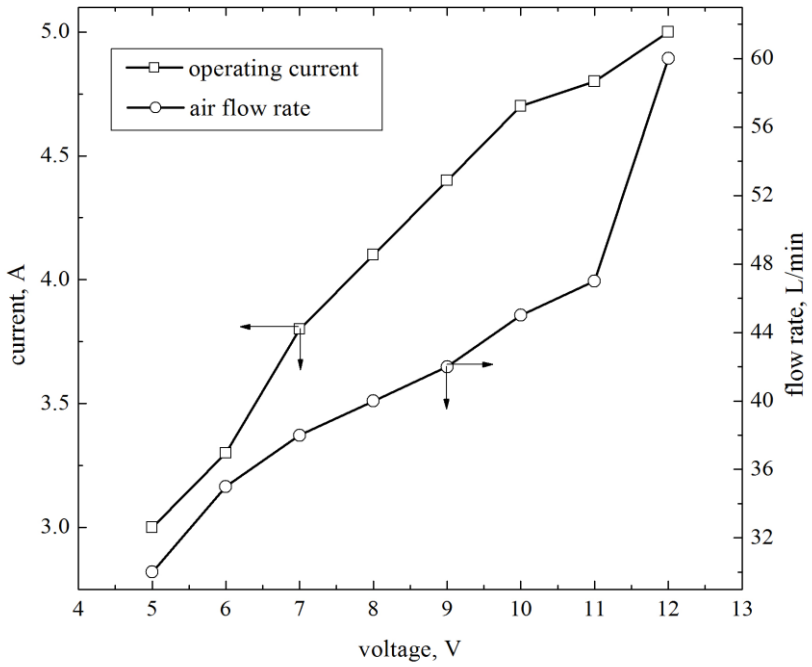

Figure 5.65 Relation of current, voltage and air flow rate of the vacuum pump.

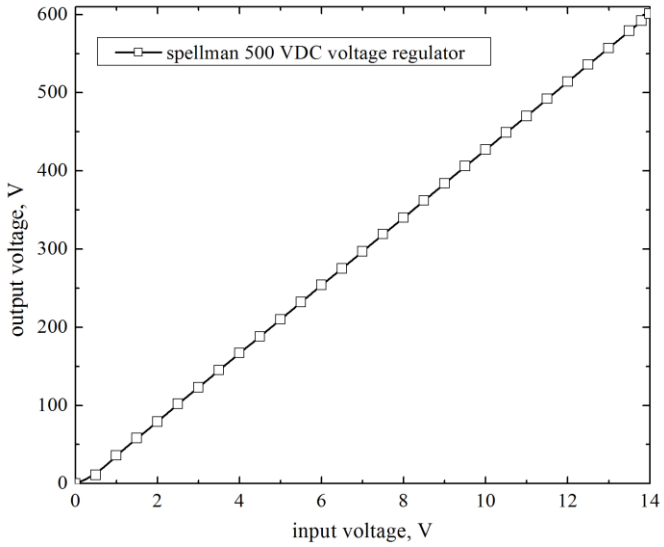

Figure 5.66 Input and output voltage of Spellman model MM0.1P0.5/12.

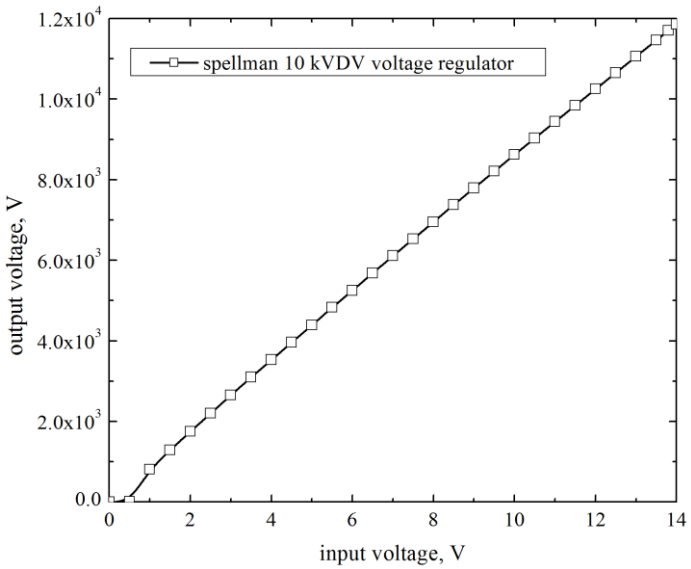

Figure 5.67 Input and output voltage of Spellman model MM0.1P1.5/12.

5.7 Field Test Comparison with Standard Detectors

5.7.1 Standard Detectors for PM10

1) The 1400a TEOM at Son Pa Mae Mho Station, Lampang. Automatic PM10 monitors series 1400a of Rupprecht & Patashnick Co., Inc., was used to compare for first field test. This device can measure only PM10 and was installed in the station at Son Pa Mae Mho, Lampang. The control room was set 25 ^{o}C temperature by alternating work of two air conditioning unit. Figure 5.68 shows 24 h of the charging current of

PM10, PM2.5, and PM1.0 on 24 June 2013. It was found that the ambient aerosol increased during 5.30 to 7.00 and 16.00 to 24.00 which is a home time of local peoples. Charger of PM1.0 and PM2.5 particle charge were in corresponding with PM10. Figure 5.69 shows a comparison of 1 h average PM10 mass concentration from the 1400a and the charge particle of PM10 from the PMx detector. The 1 h average PM10 between the charge current and the mass concentration during 22 to 30 June 2013, was used to calculate the power regression model. The relationship between the current and mass was $m_p = 46.798 I_p^{1.0623}$ with 0.8121 in regression coefficient (R^2) for 216 data, as shown in Figure 5.70. After getting a relationship between current and mass, the new data current was converted to mass by this power regression model. Figure 5.71 shows 24 h of PM10 mass concentration from the 1400a and the PMx detector. It was found that the changing trends were consistent. Figure 5.72 shows a comparison of 1 h average PM10 between the 1400a and the PMx detector during 1 to 30 July 2013. It has a 695 h average, which it was calculated that $y = 0.9173x + 1.2058$ in the reduced major axis model (RMA) with 0.6397 in R^2 of both data, as shown in Figure 5.73. After that, the 30 data were calculated for the 24 h average and compared again, as shown in Figure 5.74. The RMA model was $y = 1.0679x - 1.4284$. It was shown that the slope was near 1.0 of 1:1 line with a good R^2 at 0.8896, as shown in Figure 5.75.

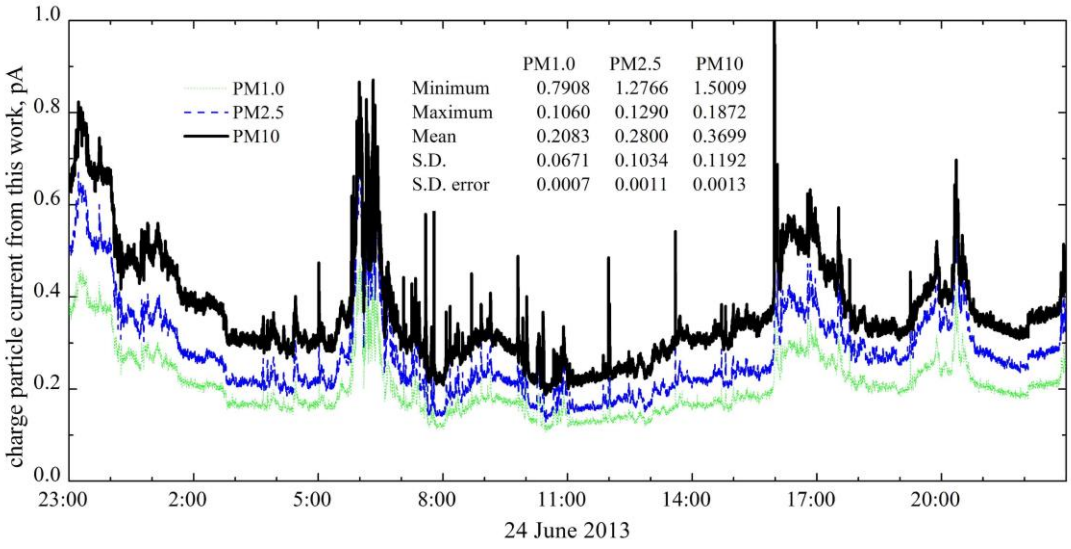

Figure 5.68 Charging current of PM10, PM2.5, and PM1.0 from the PMx detector.

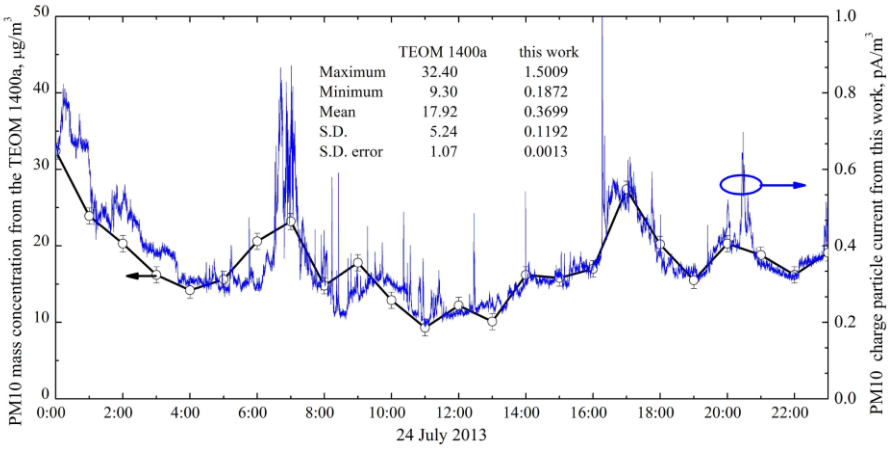

Figure 5.69 Comparison of 1 h average mass concentration from the 1400a and the charging current from the PMx detector.

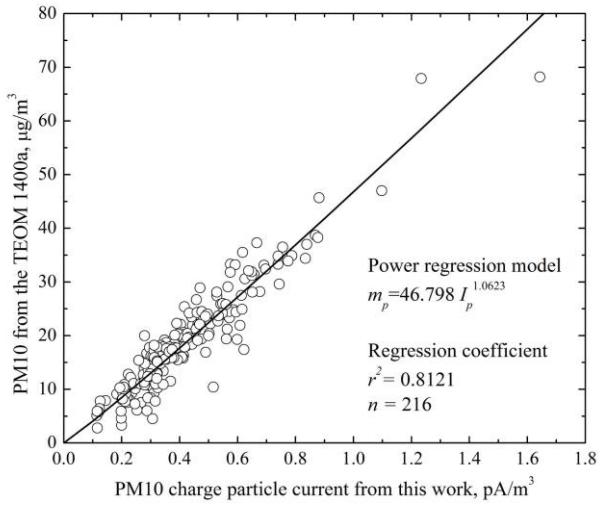

Figure 5.70 Relationship of 1 h average between the 1400a and the PMx detector.

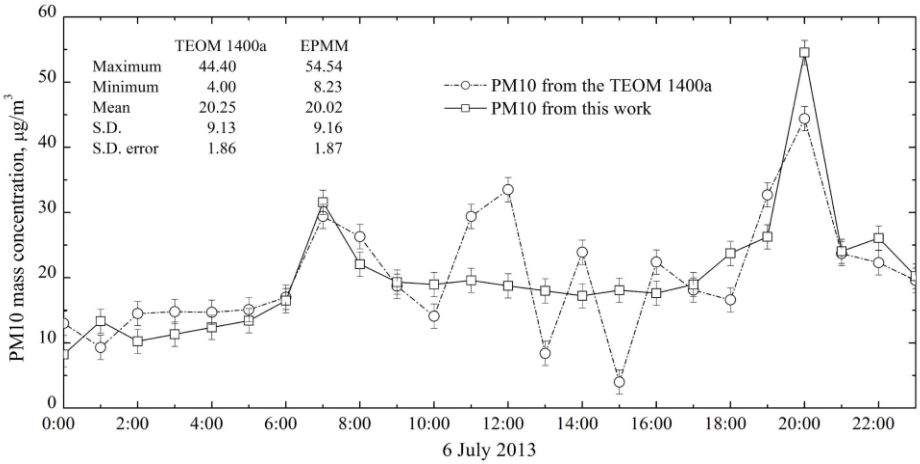

Figure 5.71 Comparison of 1 h average on 6 July 2013.

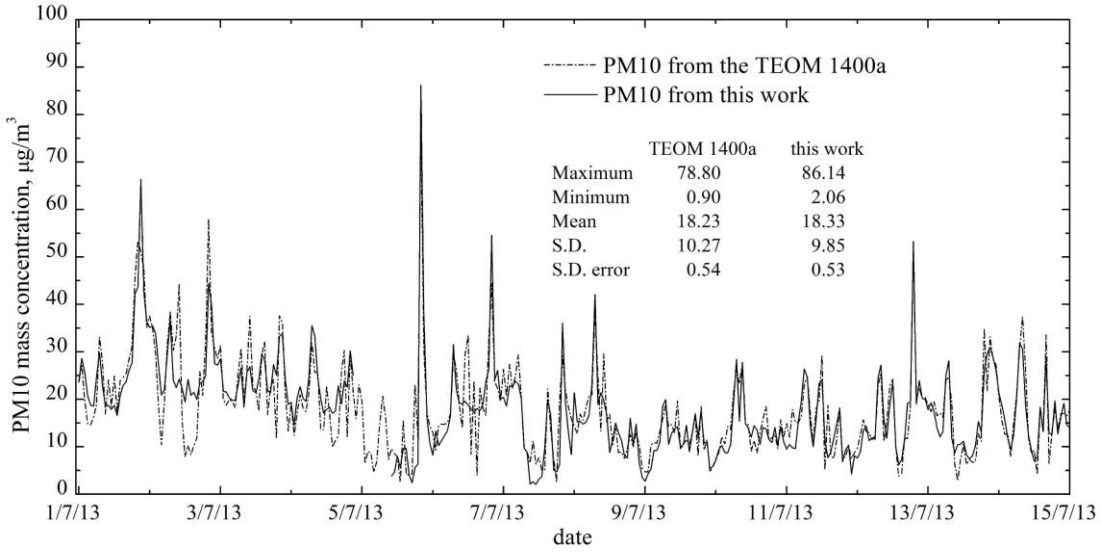

(a) 1 to 15 July 2013.

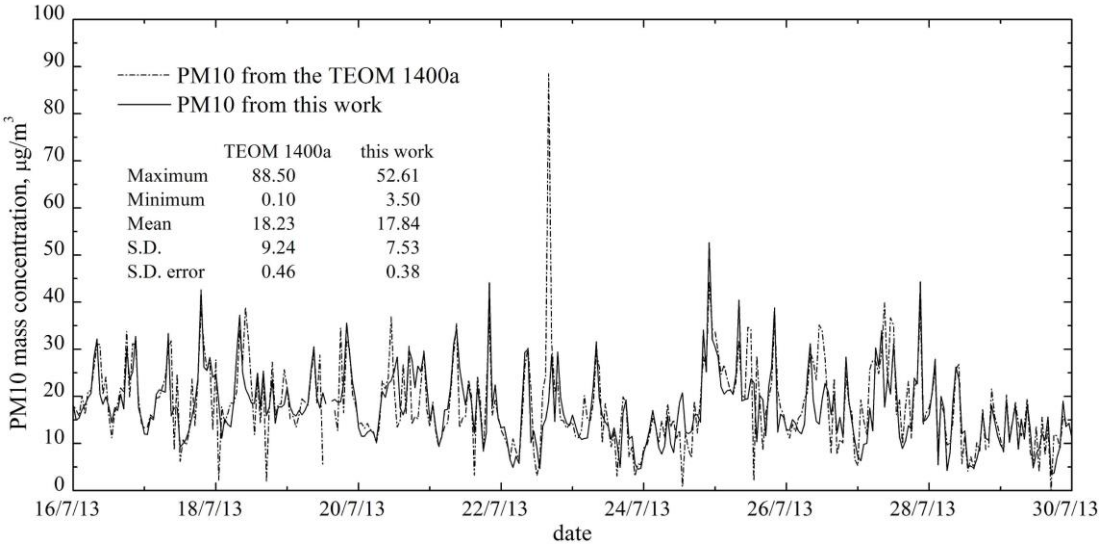

(b) 16 to 30 July 2013.

Figure 5.72 Comparison of 1 h average between the 1400a and the PMx detector.

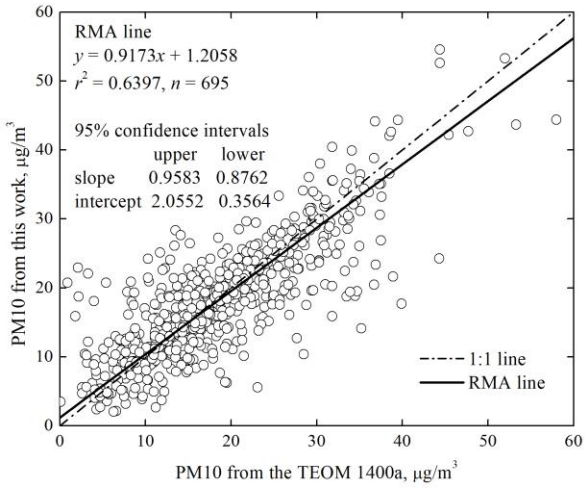

Figure 5.73 Relationship of 1 h average between the 1400a and the PMx detector.

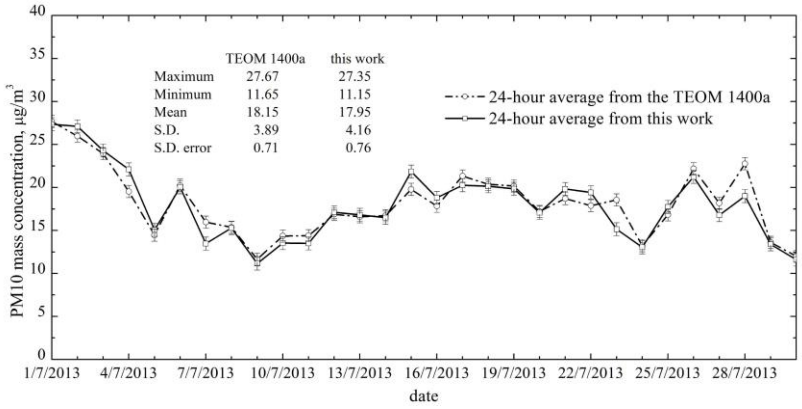

Figure 5.74 Comparison of 24 h average between the 1400a and the PMx detector.

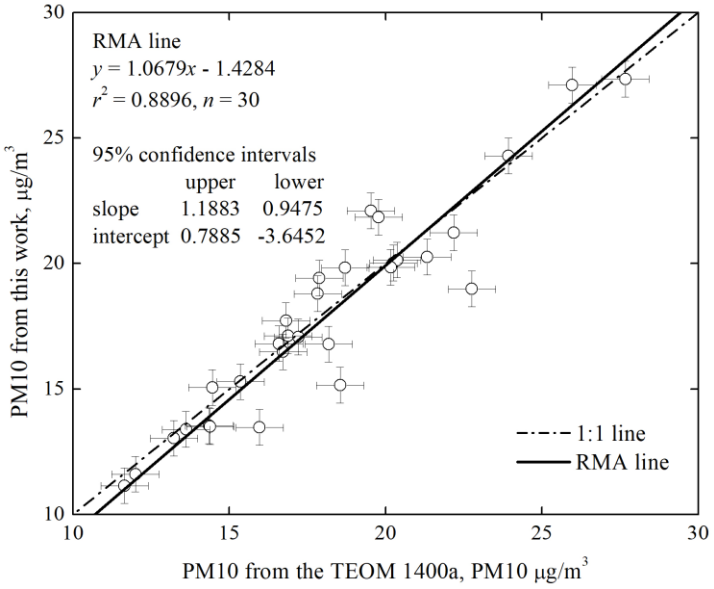

Figure 5.75 Relationship of 24 h average between the 1400a and the PMx detector.

2) The 1400a TEOM at Hoy King Mae Mho Station, Lampang. The second station for comparison test was at Hoy King Mae Mho station (Lampang). This station has an automatic PM10 monitor series 1400a from R&P Co., Inc. Figure 5.76 shows the charging current of PM10 from the PMx detector during 13 to 15 February 2014. The behavior of the charge shows high concentration during 7:00 to 10:00 and again during 18:00 to 21:00, same for all three days. Figure 5.77 shows a comparison of PM10 mass concentration from the 1400a and PM10 charging current from the PMx detector. Similar change was observed. First step, charging current and mass concentration were calculated that $m_p = 40.346 I_p^{1.6194}$ in power regression model from 160 data in 1 h average with 0.6708 in R^2, as shown in Figure 5.78. This model was used to convert a new charging current (the PMx detector) to mass concentration and compared with mass concentration from the 1400a, as shown in Figure 5.79. Figure 5.80 shows comparison of 1 h average PM10 mass concentration between the 1400a and the PMx detector during 4 March to 30 April 2014. There were 1,074 h average. It was calculated that $y = 0.8598x + 12.0864$ in RMA model with have 0.8048 in R^2, as shown in Figure 5.81. After that, the 39 data of 24 h average were calculated and compared again, as shown in Figure 5.82. It was calculated that $y = 0.9756x + 0.8011$ in the RMA model and good R^2 at 0.9779, as shown in Figure 5.83.

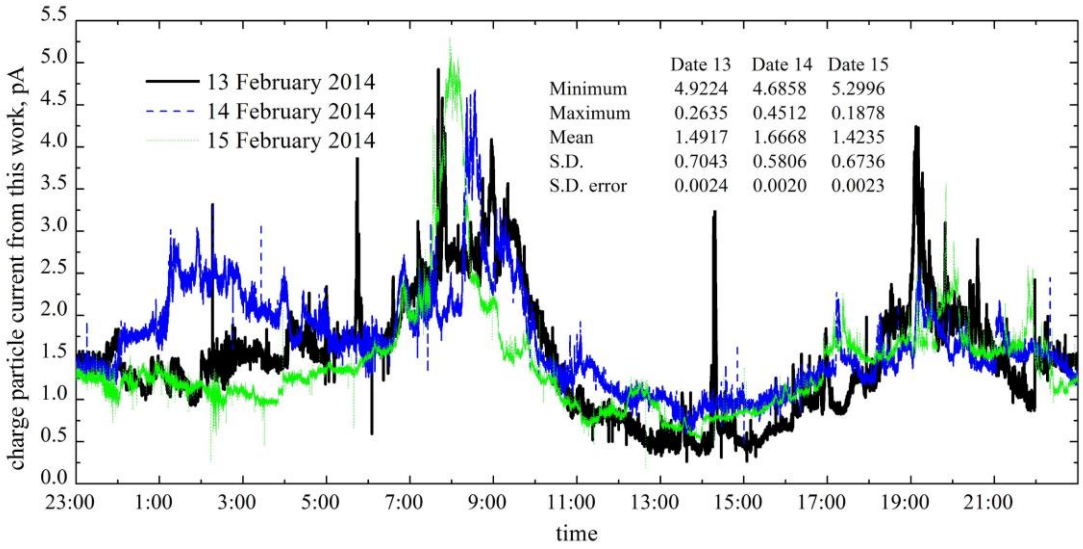

Figure 5.76 Charging current of PM10 from the PMx detector.

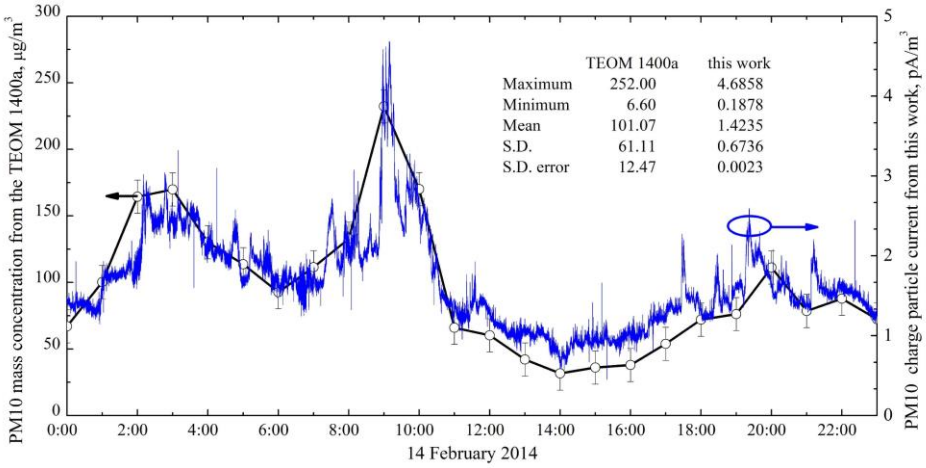

Figure 5.77 Comparison of the mass concentration
from the 1400a and the charging current from the PMx detector.

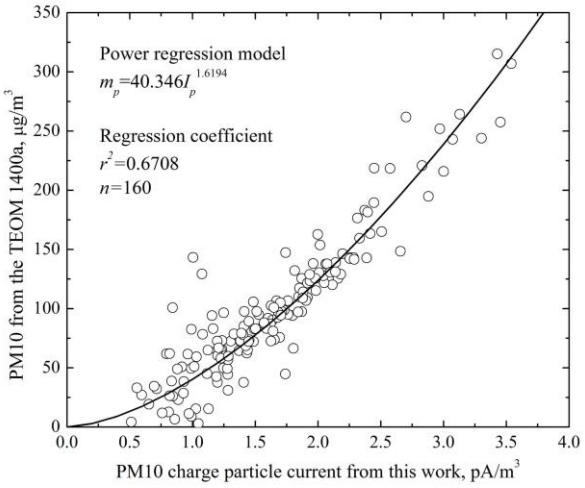

Figure 5.78 Relationship of 1 h average between the 1400a and the PMx detector.

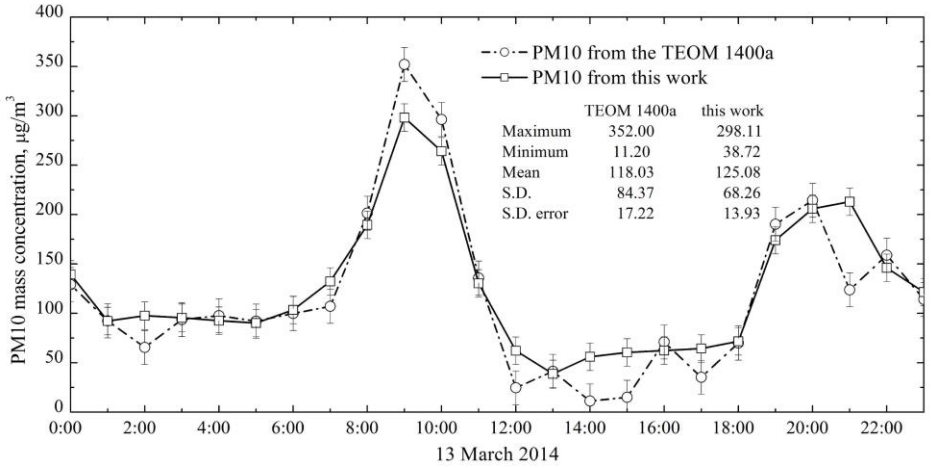

Figure 5.79 Comparison of 1 h average on 13 March 2014.

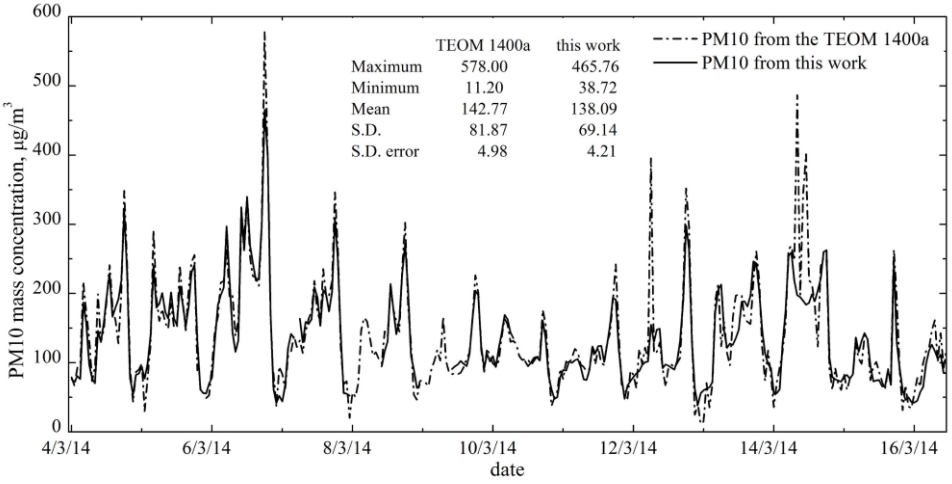

(a) 4 to 16 March 2014.

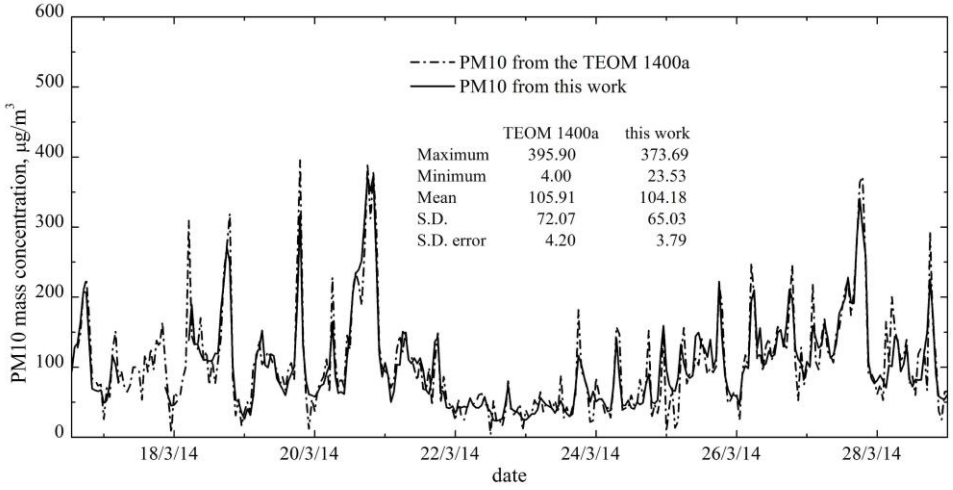

(b) 17 to 29 March 2014.

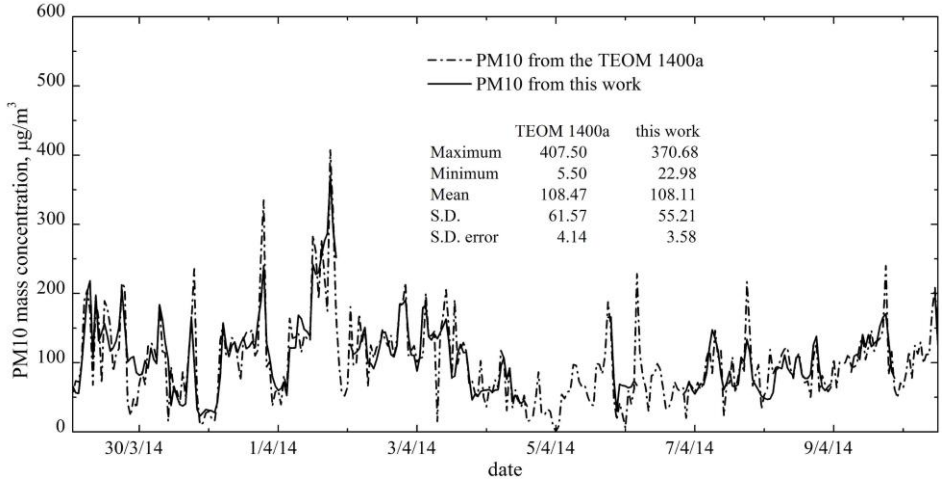

(c) 30 March to 10 April 2014.

Figure 5.80 Comparison of 1 h average between the 1400a and the PMx detector.

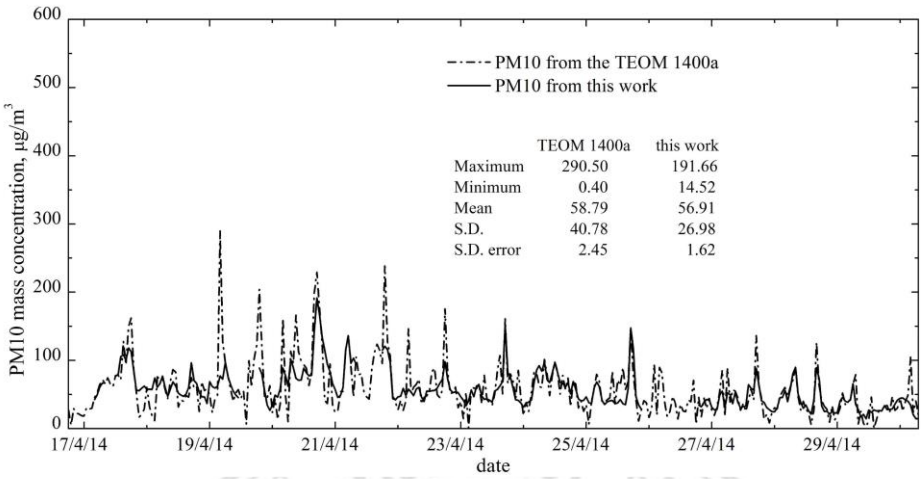

(d) 19 to 30 April 2014.

Figure 5.80 (con.) Comparison of 1 h average between the 1400a and the PMx detector.

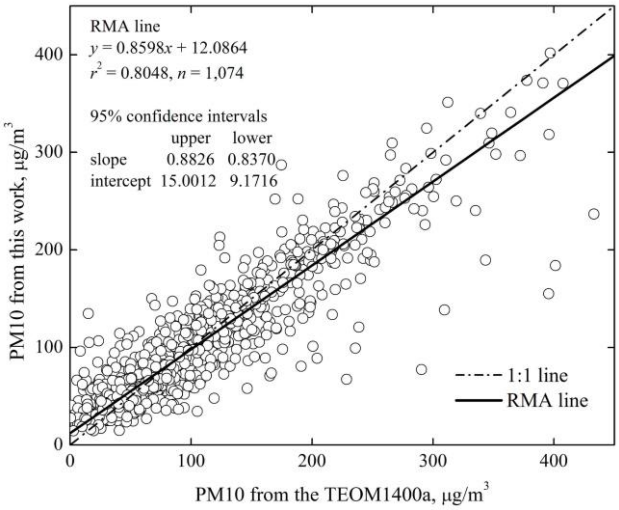

Figure 5.81 Relationship of 1 h average between the 1400a and the PMx detector.

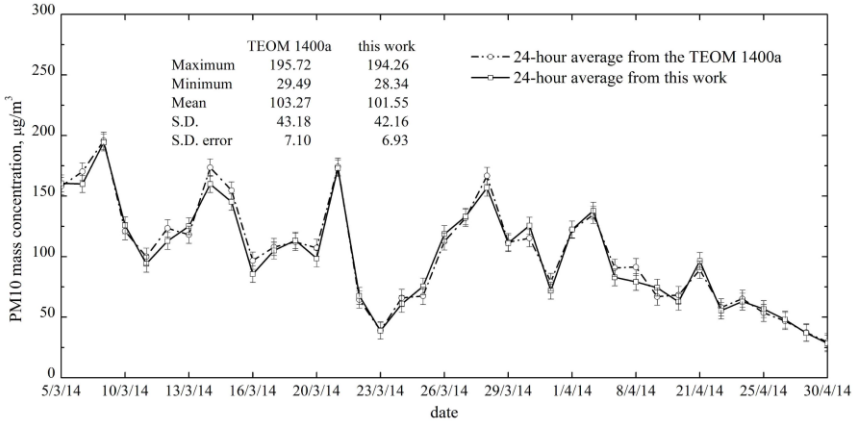

Figure 5.82 Comparison of 24 h average between the 1400a and the PMx detector.

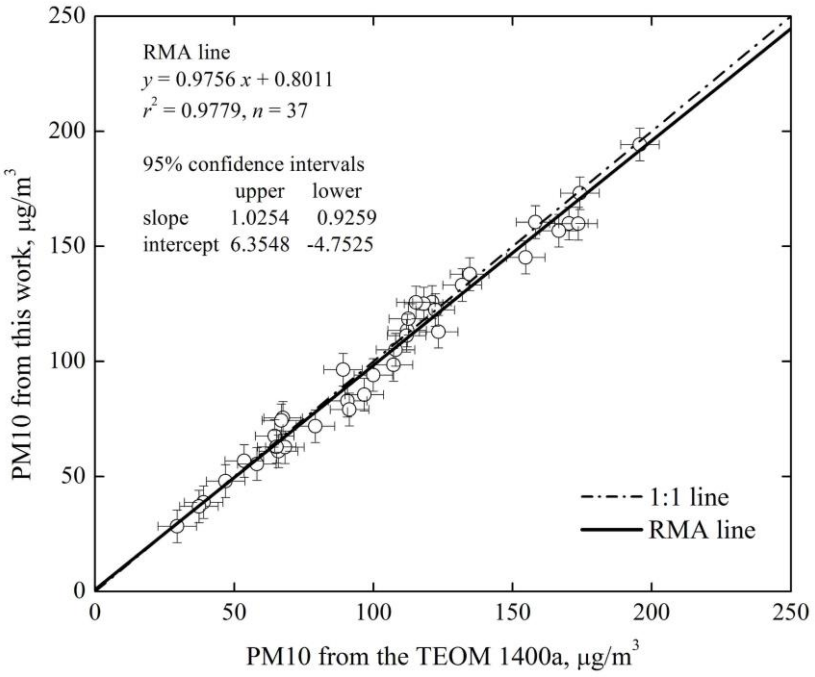

Figure 5.83 Relationship of 24 h average between the 1400a and the PMx detector.

3) The 1400a TEOM at Central Government Station, Chiang Mai. Third test of PM10 was conducted at the central government, Chiang Mai. Figure 5.84 shows the charging current from the PMx detector in 13 and 14 April 2015. The charging current signal had high swing, but stable in an average data. Some of the charging current were compared with mass concentration from the 1400a, shown in Figure 5.85. The power regression model was calculated from 135 data of 1 h average during 9 to 15 April 2015. It was found to be $m_p = 48.8751 I_p^{0.7963}$ for model with 0.7963 for R^2, as shown in Figure 5.86. Figure 5.87 shows mass concentration of 1 h average from both instruments on 18 April 2015. The data showed very similar changes. The power regression model was used for converting charging current of 1,389 in new measuring data (during 16 April to 16 June 2015) to mass concentration and compared with mass concentration from the 1400a, as shown in Figure 5.88. It was calculated that $y = 0.7411x + 9.1780$ in the RMA model with 0.8385 in R^2, as shown in Figure 5.89. The 1,389 data in 1 h average were converted to the 60 data in 24 h average mass concentration and compared, as shown in Figure 5.90. It was calculated that $y = 0.7850x + 7.3626$ in the RMA model and 0.9593 in R^2, as shown in Figure 5.91.

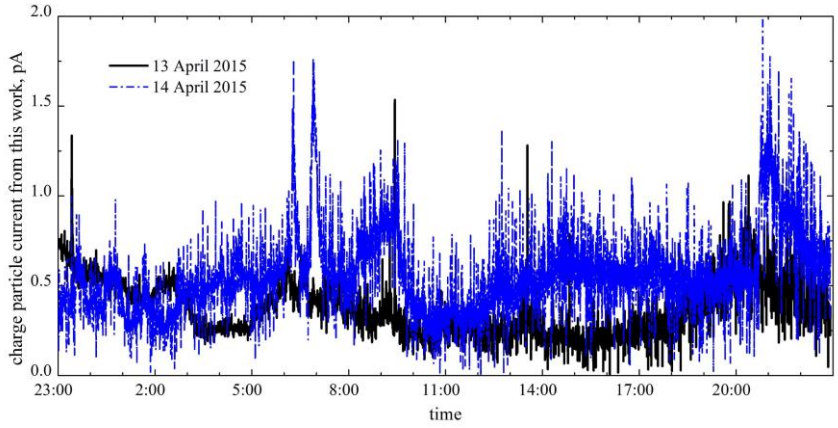

Figure 5.84 Charging current of PM10 from the PMx detector.

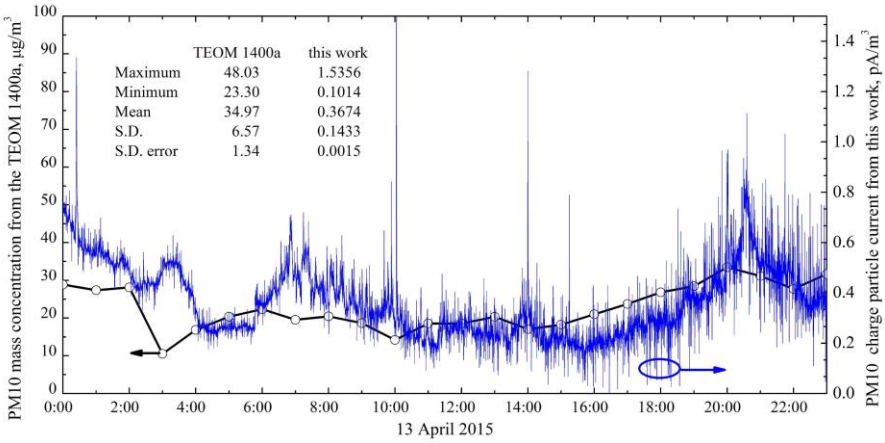

Figure 5.85 Mass concentration and charging current.

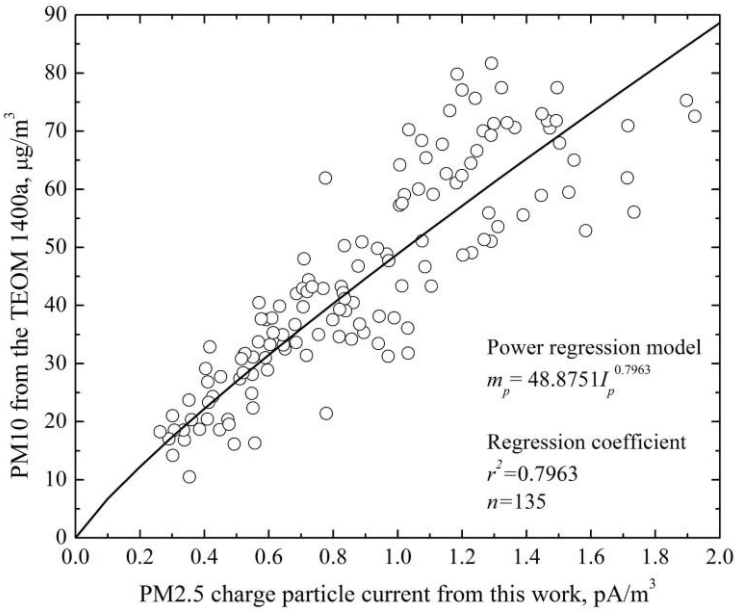

Figure 5.86 Relationship of 1 h average between the 1400a and the PMx detector.

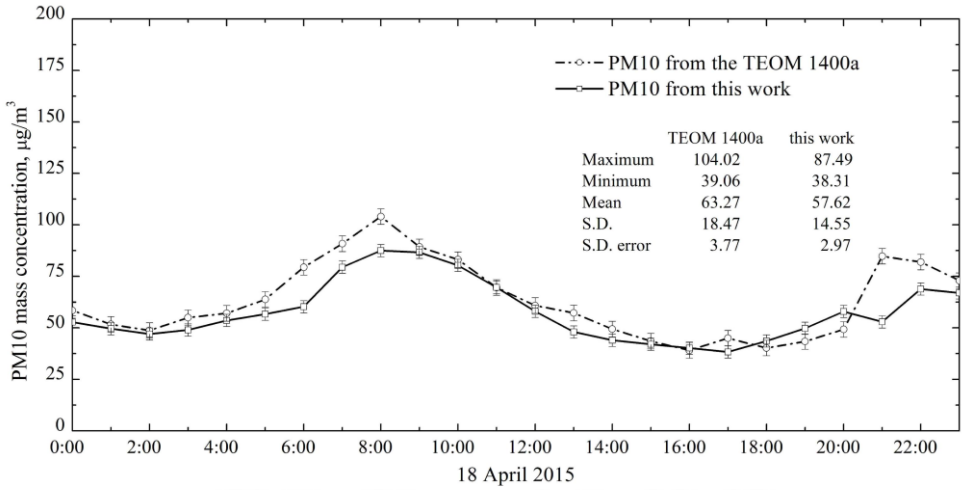

Figure 5.87 Comparison of 1 h average on 18 April 2015.

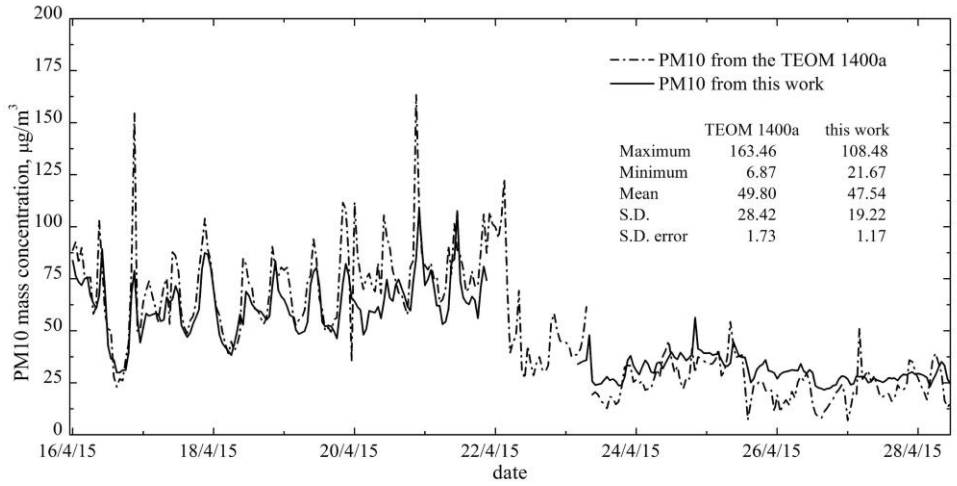

(a) 16 to 28 April 2015.

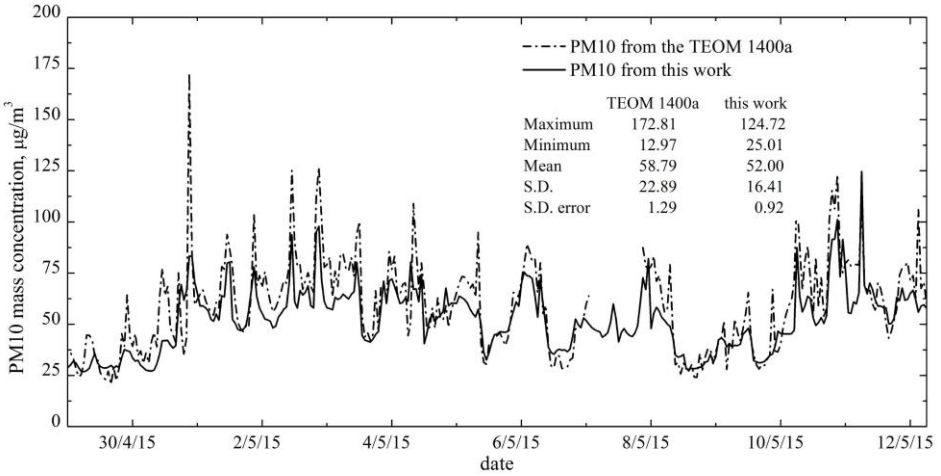

(b) 29 April to 12 May 2015.

Figure 5.88 Comparison of 1 h average between the 1400a and the PMx detector.

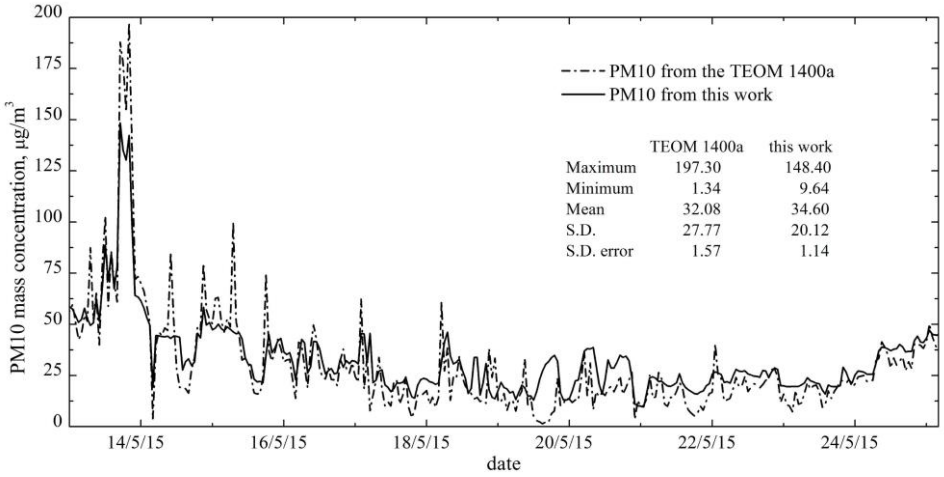

(c) 13 to 25 May 2015.

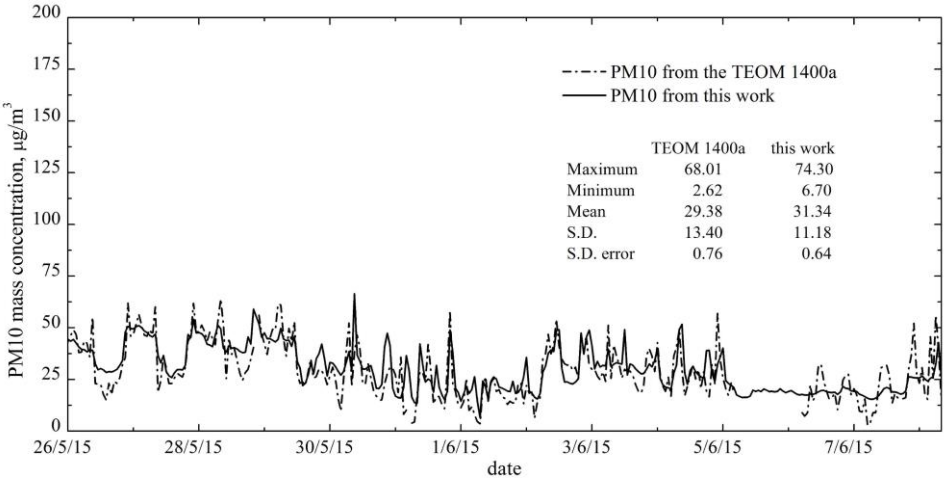

(d) 26 May to 8 June 2015.

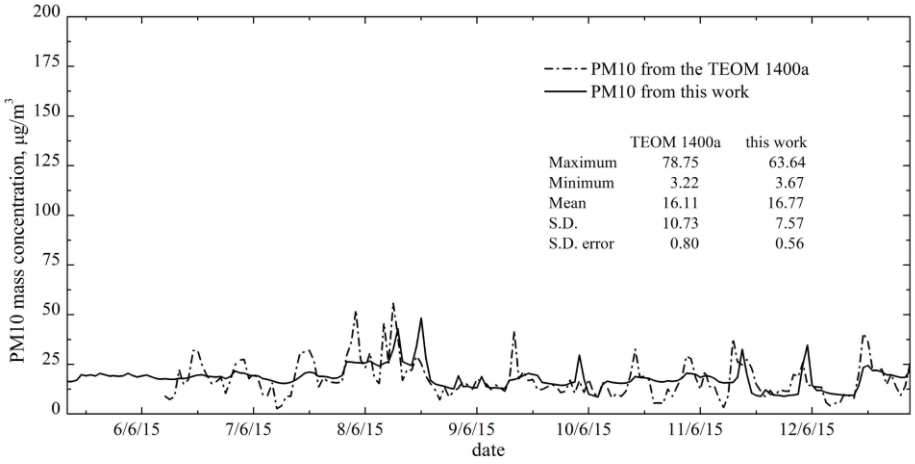

(e) 9 June to 16 June 2015.

Figure 5.88 (con.) Comparison of 1 h average between the 1400a and the PMx detector.

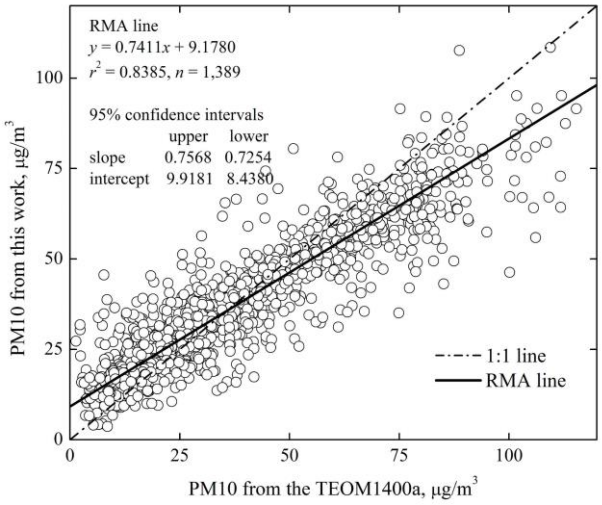

Figure 5.89 Relationship of 1 h average between the 1400a and the PMx detector.

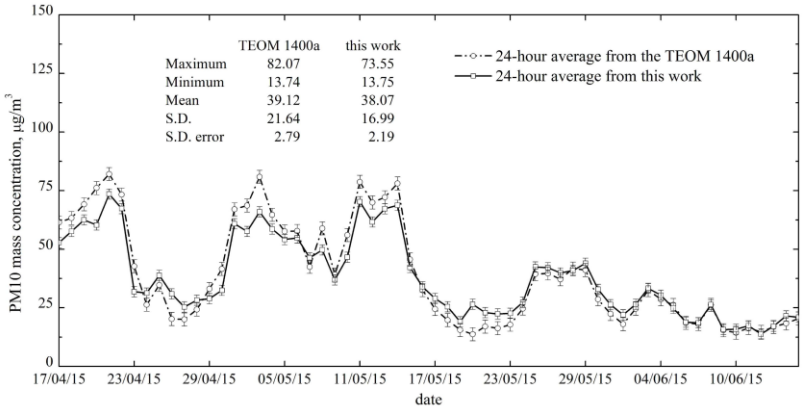

Figure 5.90 Comparison of 24 h average between the 1400a and the PMx detector.

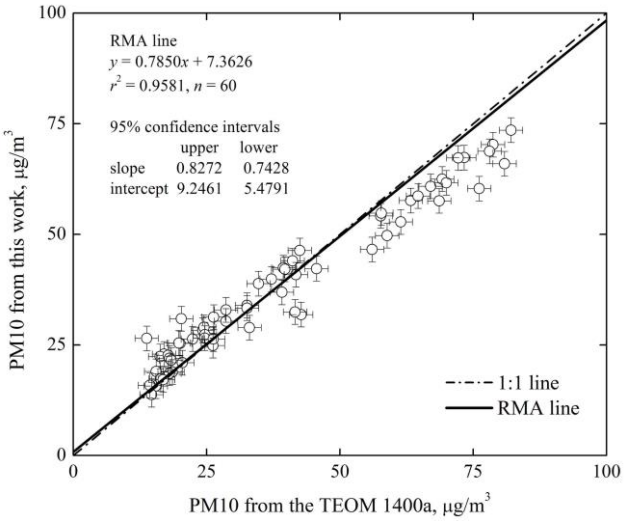

Figure 5.91 Relationship of 24 h average between the 1400a and the PMx detector.

4) The FH62C14 Beta at Yupparaj School Station, Chiang Mai. Fourth test employed the FH62C14 beta at the Yupparaj School station in Chiang Mai location. Figure 5.92 shows the charging current from the PMx detector on 9 November 2015. There was still a high swing for the charging current signal during 7.30 to 24.00. This effect may be caused by exhaust engine surrounding. Figure 5.93 shows the comparison of mass concentration from the FH62C14 and the charging current from the PMx detector. The 191 data of 1 h average from both instruments during 6 to 14 November 2015, shown in Figure 5.94 were used to find the power regression model. It was found to be that m_p =47.124$I_p^{0.7609}$ with 0.7682 in R^2 . This model was used to find mass concentration for a new data from the PMx detector during 16 November 2015 to 8 January 2016. There were 1,208 data for 1 h average. Figure 5.95 shows the comparison of 1 h average of mass concentration between the FH62C14 beta and the PMx detector on 17 December 2015. The change was very similar. The 1,208 mass concentration data of 1 h average from both instruments were compared, as shown in Figure 5.96. It was calculated that y =0.9446x +1.0690 in the RMA model with 0.8478 in R^2 as shown in Figure 5.97. Figure 5.98 is a comparison of 52 data of 24 h average from both instruments during 16 November 2015 to 8 January 2016. It was calculated that y = 0.7850x +7.3626 in the RMA model with 0.9478 in R^2 , as shown in Figure 5.99.

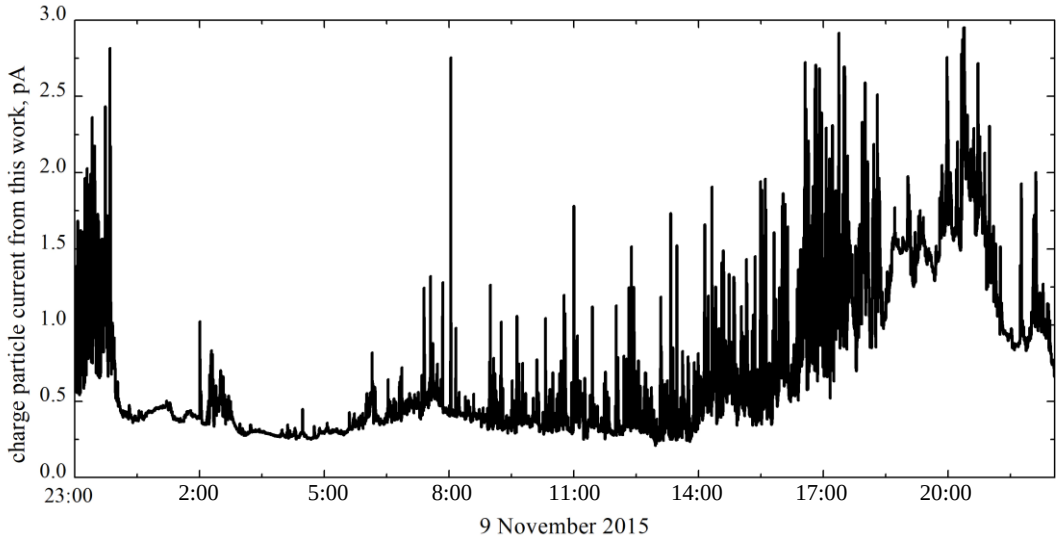

Figure 5.92 Charging current of PM10 from the PMx detector.

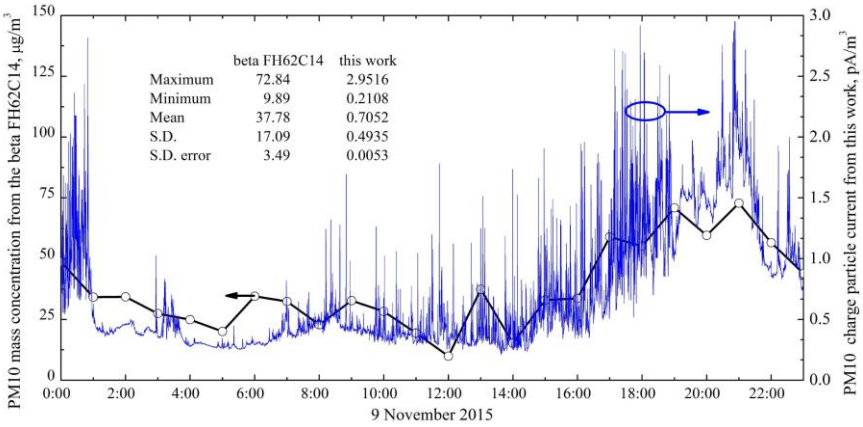

Figure 5.93 Comparison of mass concentration and the charging current.

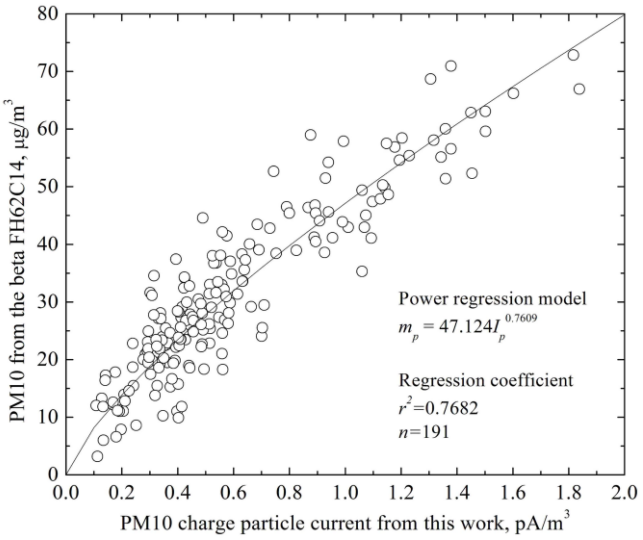

Figure 5.94 Relationship of 1 h average between the FH62C14 and the PMx detector.

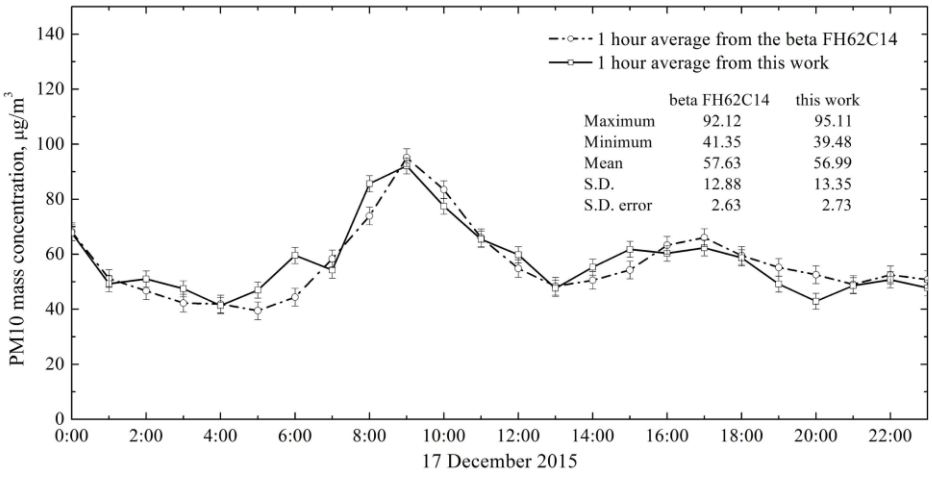

Figure 5.95 Comparison of 1 h average on 17 December 2015.

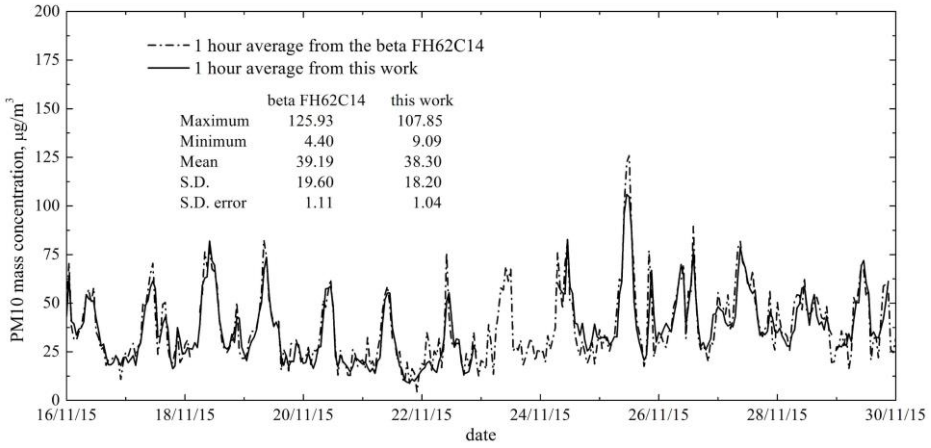

(a) 16 to 30 November 2015.

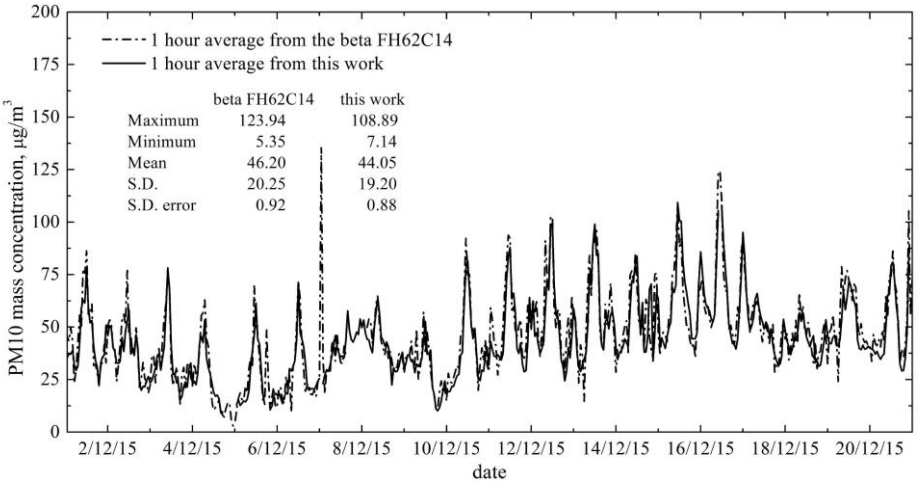

(b) 1 to 31 November 2015.

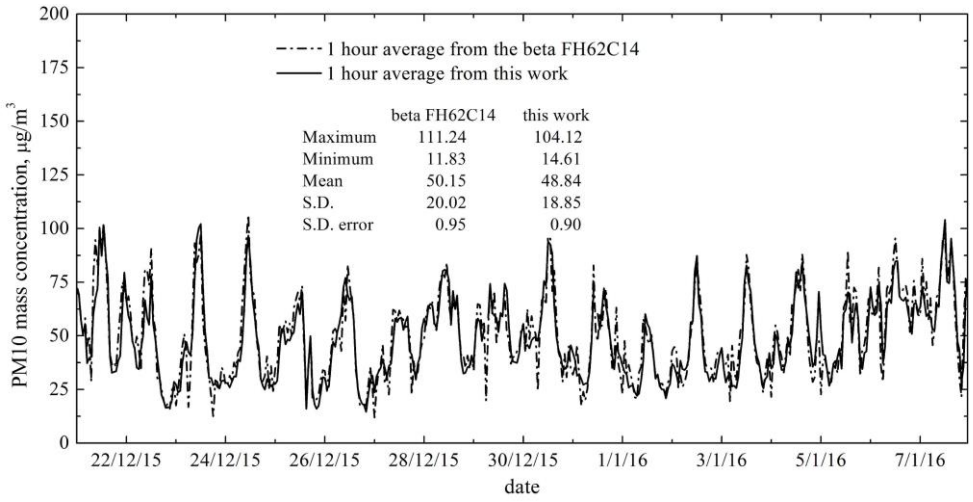

(c) 30 November 2015 to 8 January 2016.

Figure 5.96 Comparison of 1 h average between the FH62C14 and the PMx detector.

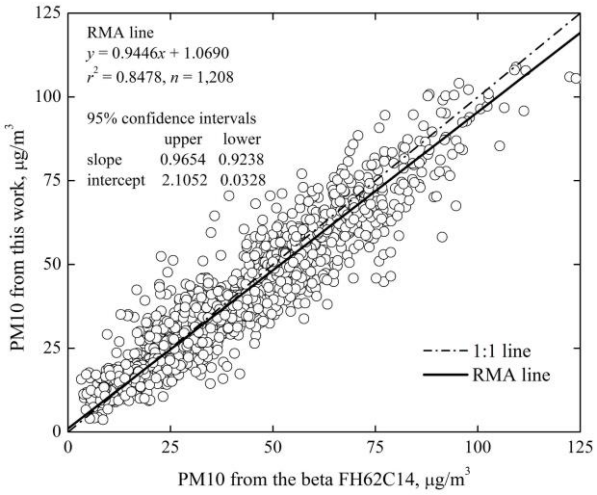

Figure 5.97 Relationship of 1 h average between the FH62C14 and the PMx detector.

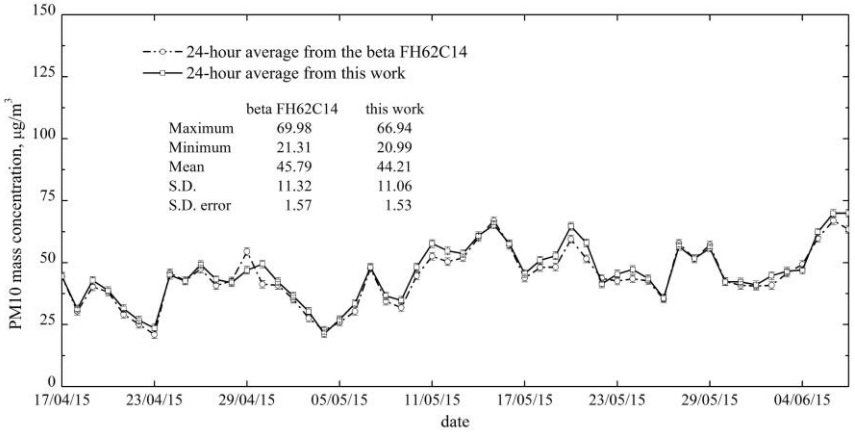

Figure 5.98 Comparison of 24 h average between the FH62C14 and the PMx detector.

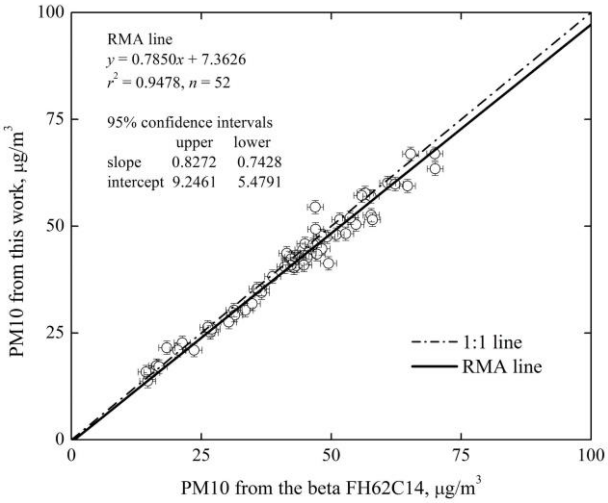

Figure 5.99 Relationship of 24 h average between the FH62C14 and the PMx detector.

5.7.2 Standard Detector for PM2.5

1) The 5014i Beta at Yupparaj School, Chiang Mai. The fifth test is a PM2.5 measurement and comparison with the 5014i beta at the Yupparaj School station in Chiang Mai location. Figure 5.100 shows the charging current from the PMx detector during 5 to 7 October 2015. There was still a high swing for the charging current signal during 7.30 to 24.00. This effect was a cause of exhaust engine surrounding, similar to PM10 measurement in the fourth test (Section 5.7.1). Figure 5.101 shows the comparison of mass concentration from the 5014i and the charging current from the PMx detector. The 106 data of 1 h average from both instruments during 5 to 9 October 2015 used to find the power regression model. It was found to be $m_p = 25.571 I_p^{0.8685}$ with 0.6639 in R^2, as shown in Figure 5.102. This model was used to finding mass concentration for a new data from the PMx detector during 15 October to 5 November 2015. There were 507 data for 1 h average. Figure 5.103 shows the comparison of 1 h average of mass concentration between the 5014i beta and the PMx detector on 22 October 2015. The change was similar. The 507 mass concentration data of 1 h average from both instruments can be compared, as shows in Figure 5.104. It was calculated that $y = 1.1258x - 2.7212$ in the RMA model with 0.8478 in R^2, as shown in Figure 5.105. Figure 5.106 is a comparison of 21 data of 24 h average from both instruments during 15 October to 5 November 2015, it was calculated that $y = 1.1253x - 2.9058$ in the RMA model with 0.9811 in R^2, as shown in Figure 5.107.

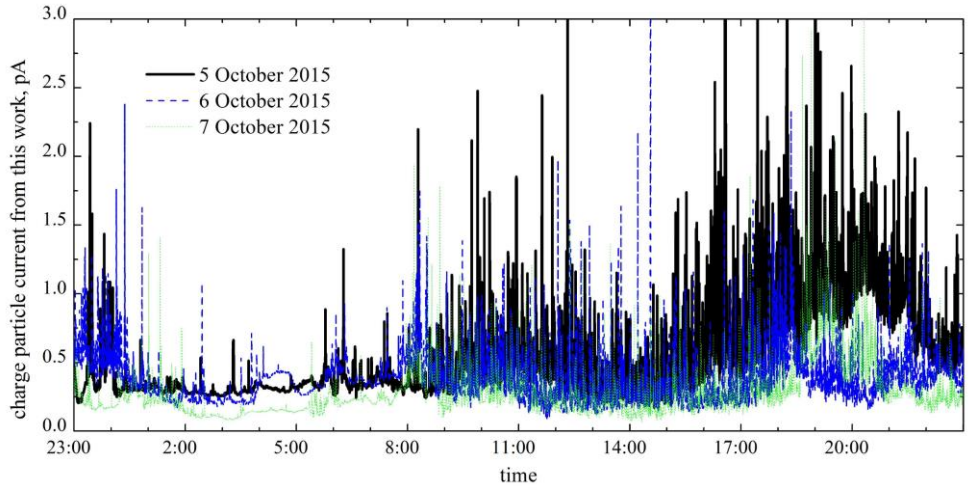

Figure 5.100 Charging current of PM2.5 from the PMx detector.

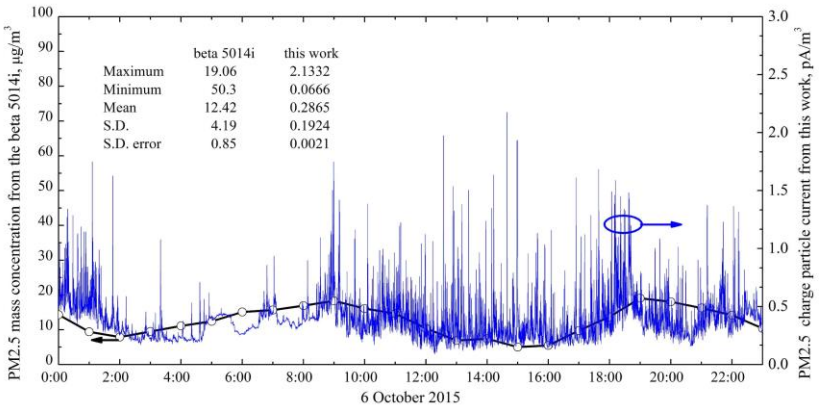

Figure 5.101 Comparison of mass concentration and charging current.

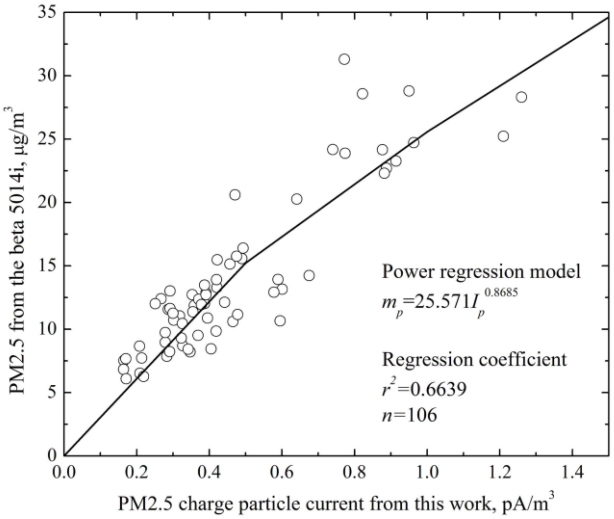

Figure 5.102 Relationship of 1 h average between the 5014i and the PMx detector.

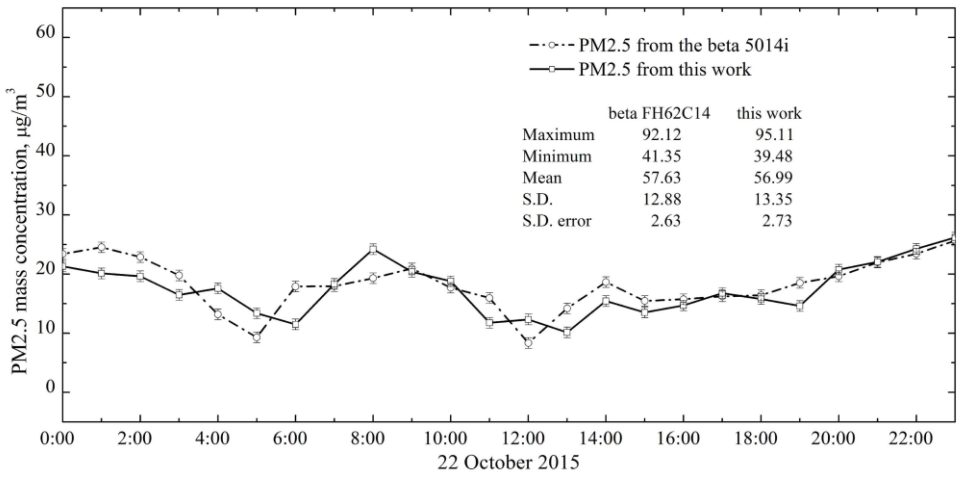

Figure 5.103 Comparison of 1 h average between the 5014i and the PMx detector.

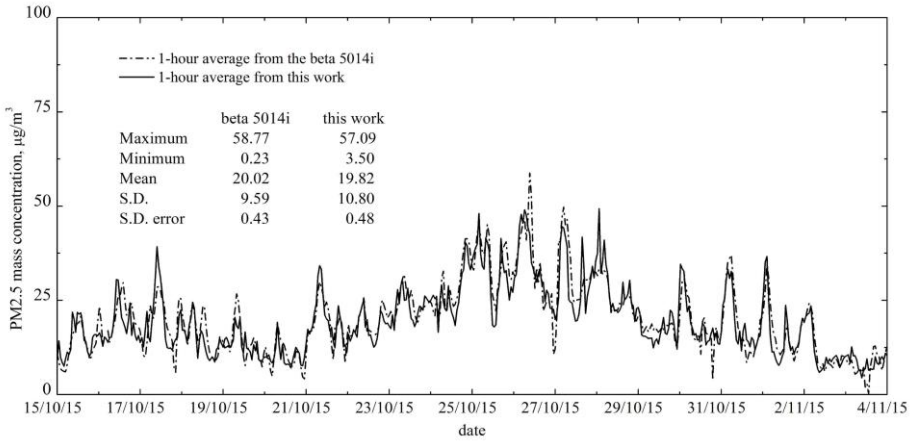

Figure 5.104 Comparison of 1 h average between 5014i and the PMx detector.

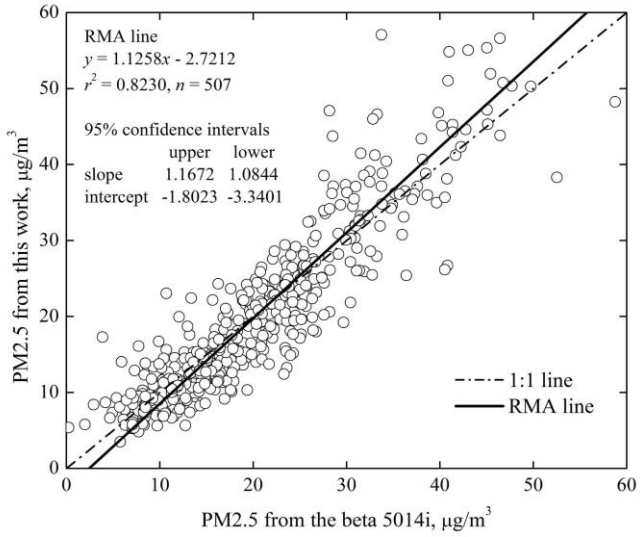

Figure 5.105 Relationship of 1 h average between 5014i and the PMx detector.

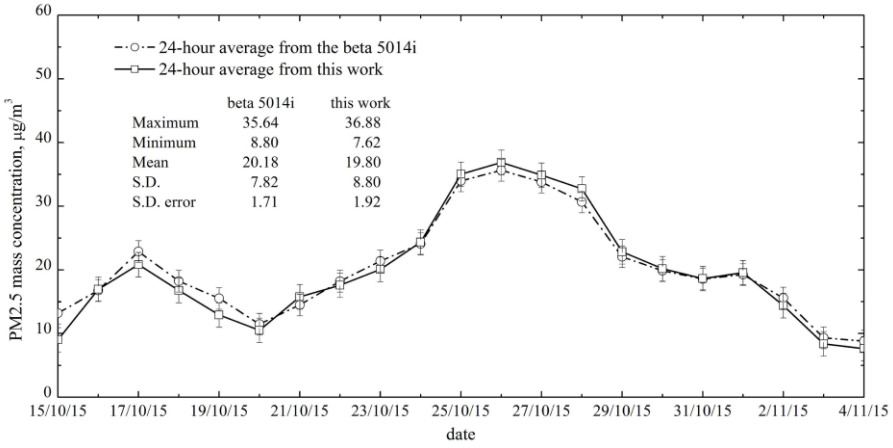

Figure 5.106 Comparison of 24 h average between the 5014i and the PMx detector.

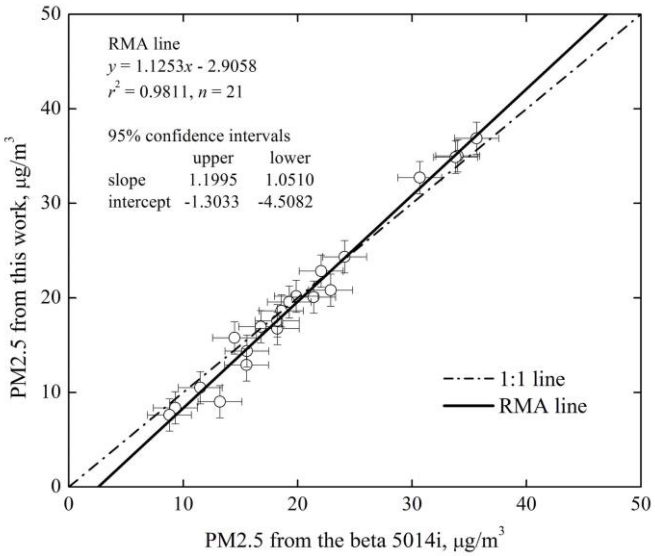

Figure 5.107 Relationship of 24 h average between the 5014i and the PMx detector.

5.7.3 Standard Detector for PM1.0

1) The 8533 TSI at Doi Saket, ChiangMai. The sixth test is a PM1.0 measurement and comparison with the 8533 TSI at Doi Saket in Chiang Mai location. Figure 5.108 shows 1-min average of PM1 mass concentration from the 8533 and the charging current from the PMx detector on 6 May 2016. Change was very similar. Figure 5.109 shows the comparison of mass concentration from the 8533 and the charging current from the PMx detector. The 1,440 data of 1-min average from both instruments during 21:00, 5 May to 20:59, 6 May 2016 were used to find the power regression model. It was calculated that $m_p = 54.769 I_p^{0.988}$ with 0.9275 in R^2. This model was used to finding mass concentration for a new data from the PMx detector during 21:00, 6 May to 12:59, 14 May 2016. There were 11,040 data for 1-min average. The 11,040 mass concentration data of 1-min average from both instruments can be compared, as shown in Figure 5.110. It was calculated that $y = 0.9877x + 0.2208$ in the RMA model with 0.9067 in R^2, as shown in Figure 5.111. Figure 5.112 is a comparison of 190 data of 1 h average from both instruments during 6 to 14 May 2016. It was calculated that $y = 0.9882x + 0.2820$ in the RMA model with 0.9435 in R^2, as shown in Figure 5.113. In addition, the comparison data for this field test were shown in Table 5.2

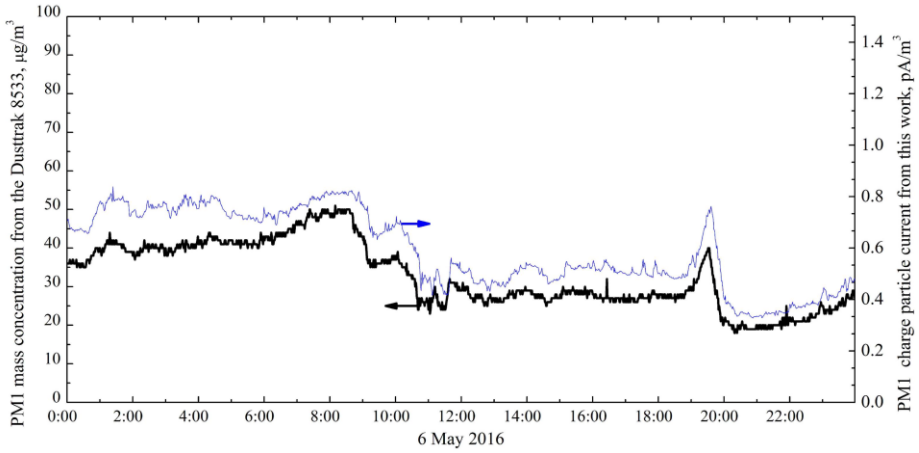

Figure 5.108 Comparison of mass concentration and charging current.

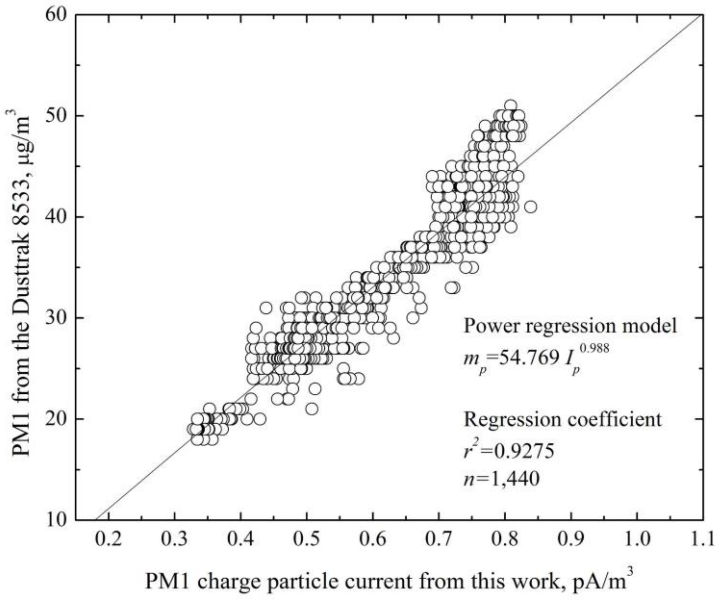

Figure 5.109 Relationship of 1 min average between 8533 and the PMx detector.

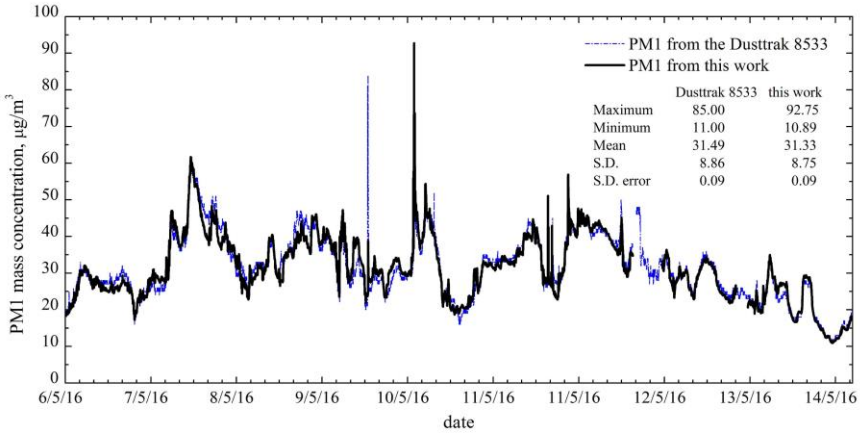

Figure 5.110 Comparison of 1 min average between the 8533 and the PMx detector.

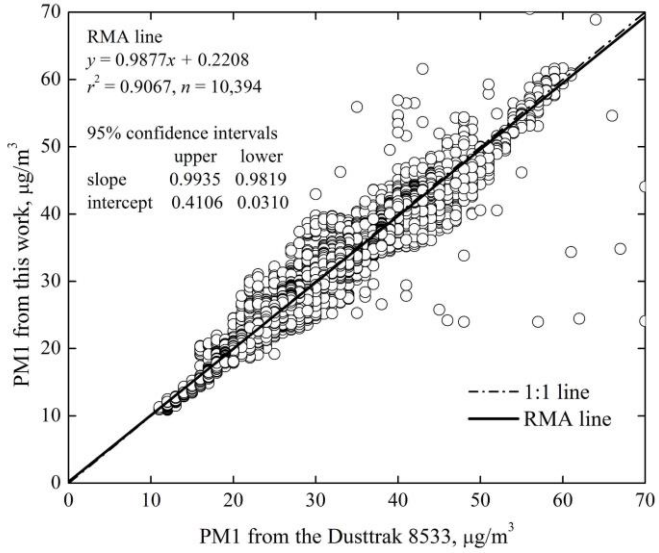

Figure 5.111 Relationship of 1 min average between 8522 and the PMx detector.

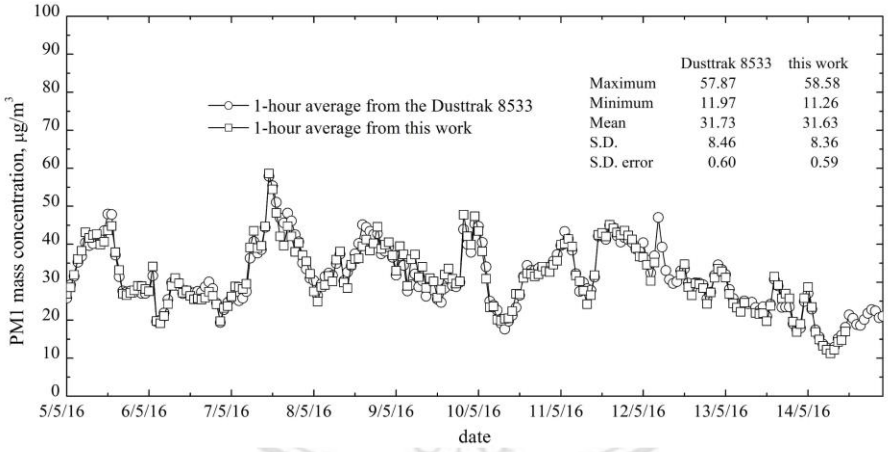

Figure 5.112 Comparison of 1 h average between the 8533 and the PMx detector.

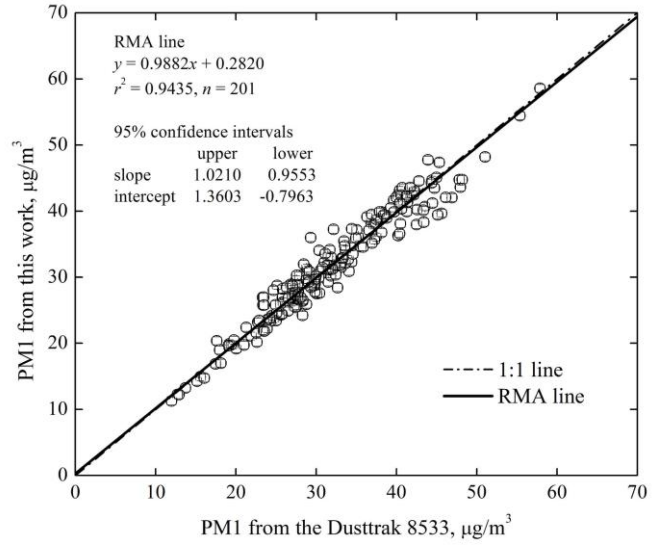

Figure 5.113 Relationship of 1 h average between the 8533 and the PMx detector.

Table 5.2 Comparison data for this field test.

Automatic PM Monitor	1400a Thermo Electric Co.	1400a R&P	1400a R&P	FH62C14 Beta Thermo Sci.	5014i Beta Thermo Sci.	DustTrak 8533 TSI Inc.
Location	Son Pa Mae Mho Station, Lampang	Hoy king Mae Mho Station, Lampang	Central Government Station, Chiang Mai	Yupparaj School Station, Chiang Mai	Yupparaj School Station, Chiang Mai	DoiSaket, Chiang Mai
PM Type	PM10	PM10	PM10	PM10	PM2.5	PM1.0
	Test1 for finding the mass conversion formula)					
Duration	22-30Jun13	13-15Feb14	9-15Apr15	6-14Nov15	5-9Oct15	5May-6May16
Average data	1 h	1 h	1 h	1 h	1 h	1 min
Data number	216	160	135	191	106	1,440
Regression coefficient (R^2)	0.8121	0.6708	0.7963	0.7682	0.6639	0.9275
Formula	$m_p = 46.79 I_p^{1.06}$	$m_p = 40.35 I_p^{1.62}$	$m_p = 48.87 I_p^{0.79}$	$m_p = 47.12 I_p^{0.76}$	$m_p = 25.57 I_p^{0.87}$	$m_p = 54.77 I_p^{0.99}$
	Test2 for recheck the formula					
Duration	1-30Jul13	4Mar-30Apr14	16Apr-16Jun15	16Nov15-8Jan16	15Oct-5Nov15	6May-14May16
Average data	1 h	1 h	1 h	1 h	1 h	1 min
Data number	695	1,074	1,389	1,208	507	11,040
Regression coefficient (R^2)	0.6397	0.8048	0.8385	0.8478	0.8478	0.9067
RMA Model	$y = 0.92x + 1.21$	$y = 0.86x + 12.09$	$y = 0.74x + 9.18$	$y = 0.94x + 1.07$	$y = 1.13x - 2.72$	$y = 0.99x + 0.22$
Average data	24 h	24 h	24 h	24 h	24 h	1h
Data number	30	39	60	52	21	190
Regression coefficient (R^2)	0.8896	0.9779	0.9593	0.9478	0.9811	0.9435
RMA Model	$y = 1.07x - 1.43$	$y = 0.98x + 0.80$	$y = 0.78x + 7.36$	$y = 0.79x + 7.36$	$y = 1.13x - 2.91$	$y = 0.99x + 0.28$